




# Constructing quadratic Lyapunov functions for conditionally stable fluid dynamics systems

Péter Tamás Nagy 

Department of Hydrodynamic Systems, Faculty of Mechanical Engineering, Budapest University of Technology and Economics, Műegyetem rkp. 3, Budapest H-1111, Hungary

**Corresponding author:** Péter Tamás Nagy, [pnagy@hds.bme.hu](mailto:pnagy@hds.bme.hu)

(Received 5 April 2024; revised 12 May 2025; accepted 17 May 2025)

This paper explores the construction of quadratic Lyapunov functions for establishing the conditional stability of shear flows described by truncated ordinary differential equations, addressing the limitations of traditional methods like the Reynolds–Orr equation and linear stability analysis. The Reynolds–Orr equation, while effective for predicting unconditional stability thresholds in shear flows due to the non-contribution of nonlinear terms, often underestimates critical Reynolds numbers. Linear stability analysis, conversely, can yield impractically high limits due to subcritical transitions. Quadratic Lyapunov functions offer a promising alternative, capable of proving conditional stability, albeit with challenges in their construction. Typically, sum-of-squares programs are employed for this purpose, but these can result in sizable optimisation problems as system complexity increases. This study introduces a novel approach using linear transformations described by matrices to define quadratic Lyapunov functions, validated through nonlinear optimisation techniques. This method proves particularly advantageous for large systems by leveraging analytical gradients in the optimisation process. Two construction methods are proposed: one based on general optimisation of transformation matrix coefficients, and another focusing solely on the system's linear aspects for more efficient Lyapunov function construction. These approaches are tested on low-order models of subcritical transition and a two-dimensional Poiseuille flow model with degrees of freedom nearing 1000, demonstrating their effectiveness and efficiency compared with sum-of-squares programs.

**Key words:** instability, nonlinear instability

## 1. Introduction

Up to a specific Reynolds number, it is widely believed that the laminar state of most shear flows is unconditionally stable (Reynolds 1895; Orr 1907; Serrin 1959). However, beyond this threshold, the behaviour of the fluid remains an open question.

In the 19th century, Lord Kelvin (F.R.S. 1887) suggested that the stability threshold amplitude decreases as viscosity approaches zero: ‘... the steady motion is stable for any viscosity, however small; and that the practical unsteadiness pointed out by Stokes forty-four years ago and so admirably investigated experimentally five or six years ago by Osbourne Reynolds, is to be explained by limits of stability becoming narrower and narrower the smaller is the viscosity’. Unfortunately, determining this permissible perturbation level of the laminar state has proven to be a challenging problem. One exception is the well-known linear stability limit, beyond which the laminar state’s region of attraction vanishes. However, for several practical applications, this limit is excessively high, if not infinite.

The literature on the conditional and unconditional stability analysis of shear flows is extensive. Here, only some relevant results are mentioned. For further details and results, the books by Joseph (1976), Drazin & Reid (2004) and Straughan (2004) are recommended.

### 1.1. *Global, unconditional stability analysis*

The initial solutions for the unconditional stability limit of plane Poiseuille flow were derived by Reynolds (1895) and Orr (1907). Initially, solutions were obtained for the two-dimensional problem due to its complexity. However, the computed Reynolds number,  $Re = 88$  – defined using the maximum velocity and half the channel gap – was an order of magnitude smaller than the value observed experimentally. Later, Joseph & Carmi (1969) tackled the three-dimensional problem and revealed that the kinetic energy of spanwise oscillating perturbations could grow at a significantly smaller Reynolds number, specifically 49.55. Additionally, they demonstrated that the critical perturbations of two-dimensional base flows were those oscillating exclusively in the spanwise direction, instead of in the streamwise one.

Goulart & Chernyshenko (2012) proposed that to prove global stability there is no better alternative than kinetic energy among quadratic functions in the case of a general flow. At the same time, many attempts were made to add reasonable assumptions and constraints on the solutions in order to prove the global stability of the flow up to higher Reynolds numbers, even though they are not mathematically rigorous.

Falsaperla, Giacobbe & Mulone (2019) introduced a modified kinetic energy and assumed the perturbations to be two-dimensional tilted waves. They varied the angle between purely streamwise and purely spanwise oscillating waves and proposed that purely streamwise oscillating waves emerge as the most critical. Their findings in the case of tilted waves were in excellent agreement with experiments conducted by Prigent *et al.* (2003) for plane Couette flow. Moreover, their results aligned with the work of Joseph & Tao (1963) and Moffatt (1990), who independently established the stability of flow perturbed by spanwise oscillating waves.

A further generalisation of the kinetic energy was recently investigated by Nagy & Kulcsár (2023), who introduced multipliers in the definition of kinetic energy for all velocity components. Addressing the three-dimensional domain, they predicted a critical Reynolds number roughly 25 % larger for both Couette and Poiseuille flows. Their analysis indicated that critical perturbations manifest as tilted waves in both flow configurations. However, it is worth noting that their study neglected a nonlinear term in the pressure

calculations, limiting its validity to a specific perturbation amplitude; this limit, however, was not determined.

Another way of improving the original energy method involves constraining the potential perturbation field rather than altering the definition itself. Originally, such a constraint was that the velocity field must satisfy the continuity equation, implying divergence-free velocity in the context of incompressible flow. Nagy, Paál & Kiss (2023) observed that the solution of the Reynolds–Orr equation fails to meet the compatibility condition essential for a smooth, physically realistic solution. They introduced this condition as a constraint into the problem; however, their ultimate finding was that, while the solution of the Reynolds–Orr equation does not meet the condition, there exist velocity fields close to the solution that do fulfil the compatibility condition. This implies that, in the cases considered, introducing the condition does not change the energy stability limit.

An alternative approach to enhancing the Reynolds–Orr method and proving global stability involves the utilisation of enstrophy. Synge (1938) explored this method, and more recently, Fraternale *et al.* (2018) applied it, predicting a significantly larger critical Reynolds number of  $Re_{crit} = 155$  for two-dimensional Poiseuille flow. Notably, this value is approximately double the energy limit for the same configuration. Unfortunately, the nonlinear term in the vorticity equation cannot be eliminated in the case of three-dimensional flows. Furthermore, Nagy (2022) showed that, in the case of three-dimensional systems, the predicted critical Reynolds number is smaller than in the case of using the original Reynolds–Orr equation even if the nonlinear terms are neglected, which confirms the statement of Goulart & Chernyshenko (2012) that the kinetic energy is the optimal choice for proving global stability among quadratic functions.

Alternatively, higher than quadratic-order functionals can be utilised for proving the global stability of the laminar state. Galdi & Straughan (1985) showed possible analytical ways to construct such an energy function to prove global or local stability. They demonstrated the conditional stability in the case a basic model for the motion of microorganisms.

Goulart & Chernyshenko (2012) suggested that the global stability of the laminar state can be proved at a higher Reynolds number than  $Re_E$  by utilising higher-order polynomials as Lyapunov functions. The usage of sum-of-squares (SOS) programs is proposed to create such a function. They demonstrated its effectiveness on a ninth-order model of Couette flow. Unfortunately, the computational needs of the method increase rapidly with the degrees of freedom of the investigated system. Therefore, they proposed a so-called infinite-dimensional model to investigate the stability of a flow governed by partial differential equations, employing only a finite number of state variables while ensuring the global stability of the original infinite-dimensional system is preserved. As the first step, their method uses a Galerkin projection to create a low-order system up to a finite number of modes. In the next step, instead of neglecting the truncated modes, they took into account this tail. Utilising linear eigenvalue problems, the worst-case effect of the tail can be estimated on the stability of the infinite-dimensional system. Later, Huang *et al.* (2015) applied the method to the rotating Couette flow and improved the global stability limit compared with the standard kinetic energy method. Fuentes, Goluskin & Chernyshenko (2022) employed this optimisation technique to create non-quadratic Lyapunov functions of planar Couette flow and gave a sharper bound on the effect of the tail. They projected the velocity field onto the modes of the classic energy equation solutions and achieved a significantly higher Reynolds number limit using 13 modes.

### 1.2. Local, conditional stability analysis

Alternatively, a quadratic energy functional can be used to prove stability up to a certain threshold. Galdi & Padula (1990) showed a possible way to construct a generalised energy functional by decomposing the linear operator of the governing equation. They argued that the non-symmetry of the operator can have a stabilising effect and presented ways to include this effect in the energy functional. They applied the method to Bénard convection and various rotating flows.

Similarly, a quadratic energy function was proposed by Nerli, Camarri & Salvetti (2007) by perturbing the original norm. They calculated the threshold amplitude of low-dimensional transition models numerically utilising a nonlinear optimisation method. Here, their work is followed, but the quadratic energy is defined in a general form through a transformation matrix. The optimisation is discussed in detail and improved, and the method is extended to significantly larger systems. The method, which defines quadratic kinetic energy using a transformation matrix and validates it as a conditional Lyapunov function through nonlinear optimisation, is referred to as the generalised kinetic energy (GKE) method.

Sum-of-squares programs can also be utilised to construct conditional Lyapunov functions for finite-dimensional models and to estimate the threshold amplitude. Jarvis-Wloszek (2003) proposed two algorithms: the ‘expanding D algorithm’ and ‘expanding interior algorithm’. The simplified version of the second one is widely used for low-order dynamical systems (Tan & Packard 2008; Topcu, Packard & Seiler 2008; Khodadadi, Samadi & Khaloozadeh 2014; Meng *et al.* 2020). Kalur, Seiler & Hemati (2021) applied this approach to low-dimensional models of subcritical transition. An alternative SOS program for constructing conditional Lyapunov functions was defined by Liu & Gayme (2021), who applied it to various low-dimensional models. These two approaches will be compared in this study based on computational time and threshold amplitudes.

The conditional stability can also be proved by bounding the nonlinear terms. One promising approach is to regard the nonlinear part as an excitation and establish a bound for it, thus obtaining conditional stability. This concept was explored in the context of Couette flow using the resolvent of the linear operator in the unstable half-plane by Kreiss, Lundbladh & Henningson (1994). However, extending this solution method further appears to be challenging. Another, more comprehensive method that models the nonlinear term as a bounded excitation of the linear system has been developed by two groups: Liu & Gayme (2020) and Kalur *et al.* (2021), referred to as the quadratic constrained (QC) method. They applied this technique to low-dimensional models of subcritical transition. The approach proved to be computationally efficient, but the predicted threshold amplitude is significantly lower than in the case of SOS methods. A similar bounding to the nonlinear terms was applied to low-dimensional flow models by Toso, Drummond & Duncan (2022), utilising matrix inequalities, and they calculated roughly 30 % higher threshold amplitude than the aforementioned QC method.

A fundamentally different approach to address this problem involves calculating the perturbation with minimal energy necessary to induce a non-laminar solution, often referred to as the minimal seed (Pringle, Willis & Kerswell 2012). This approach is similar to conditional stability calculations; however, in this methodology, optimisation occurs on the unstable side of the boundary between stable and unstable regions of the laminar state. The conditional Lyapunov functions maximise the perturbation kinetic energy until the point where the laminar flow remains stable, while solving the minimal seed problem provides the lower kinetic energy limit leading to another state. Implicitly, the existence and realisation of these minimal seeds demonstrate stability, as the laminar flow must

remain stable below the perturbation amplitude of the minimal seed. Unfortunately, the solution of the minimal seed problem is usually obtained by a local optimiser, and proving it to be a global optimum requires an alternative method or approach.

Typically, the initial kinetic energy is minimised, leading to maximal kinetic energy after a certain time horizon. For low-order flow models proposed by Waleffe (Waleffe 1995, 1997), Cossu (2005) calculated the energy of these minimal seeds. Later, this method was applied to real flow configurations (Rabin, Caulfield & Kerswell 2012; Duguet *et al.* 2013; Kerswell, Pringle & Willis 2014; Cherubini, De Palma & Robinet 2015; Kerswell 2018; Vavaliaris, Beneitez & Henningson 2020; Parente *et al.* 2022; Wu 2023; Zhang & Tao 2023). Nonlinear optimisations revealed localised perturbation fields with significantly lower kinetic energy than perturbations optimised by linear methods. Readers are referred to the cited papers for a more detailed discussion and specific results.

Alternatively, Pershin, Beaume & Tobias (2020) proposed a probabilistic approach to describe the boundary of the basin of attraction of the laminar state. They perturbed the laminar state of Couette flow at 40 different perturbation levels with 100 initial states per energy level, calculating the relaminarisation probability as a function of the perturbation level. Later, Pershin *et al.* (2022) suggested a Bayesian approach to compute relaminarisation probabilities with fewer simulations.

While a probabilistic approach is practically useful, determining the exact boundary of the laminar state's basin of attraction remains a significant scientific challenge. Minimal seeds calculated by various research groups for the same flow configuration exhibit similar qualitative structures, suggesting they may represent the global minimum. However, improving Lyapunov function construction is essential for validating these results and better describing the laminar state's region of attraction.

The primary objective of this study is to develop a method for constructing a conditional Lyapunov function for low-dimensional flow models that is computationally more efficient than state-of-the-art SOS techniques and applicable to significantly larger dynamical systems. At the same time, the predicted threshold amplitude remains comparably accurate. This work builds upon and improves the method introduced by Nerli *et al.* (2007). In particular, the energy is defined in a more general form using a transformation matrix, whereas Nerli *et al.* (2007) employed a less general, perturbed matrix for this purpose. Additionally, the optimisation aspect of the method is discussed in detail.

First, the classical energy method for discretised fluid mechanical systems is presented in § 2.1. Then, the generalised kinetic energy is introduced through a variable transformation using a matrix, as described in § 2.2.

The optimisation technique used to identify the worst-case perturbations and to compute the region of attraction of the laminar state is described in detail in § 2.2.2. Several gradient-based optimisation algorithms are compared. Next, two strategies for optimising the transformation matrix are presented in § 2.3 to obtain the optimal generalised energy. One of them involves optimising the elements of the transformation matrix to maximise the region of attraction, while the other method utilises only the decomposition of the eigenvalue matrix of the linearised system. Next, the method is compared with state-of-the-art techniques utilising SOS programs in § 2.4.

Later, the method is applied to low-dimensional models of subcritical transition: the Trefethen two-dimensional TTRD' model (Baggett & Trefethen 1997) and the Waleffe (1995) (W95) model (§ 3.1). As a last step, the new technique is demonstrated for higher, yet still relatively low-order (few hundred degrees of freedom) models of the two-dimensional Poiseuille flow (§ 3.2). These models are created using the Galerkin projection method, employing the Stokes eigenfunctions. Finally, the findings and conclusions are summarised in § 4.

## 2. Theory

### 2.1. The original energy method

After projecting the perturbed Navier–Stokes equation on an  $L^2$  orthogonal and divergence-free basis, the fluid motion can be described by the following truncated ordinary differential equation system

$$\frac{dq_i}{dt} = A_{ij} q_j + Q_{ijk} q_j q_k, \quad (2.1)$$

where  $q_i(t)$  represents an  $n$ -element vector ( $i = 1, \dots, n$ ) describing the perturbation of the base flow as a function of time  $t$ . The coefficients  $A_{ij}$  and  $Q_{ijk}$  are time-independent arrays characterising the behaviour of the perturbed flow, where  $i, j$  and  $k$  are running variables ranging from 1 to  $n$  in the Einstein summation notation. The state at the origin is stable if the perturbations ( $q_i$ ) tend to zero as  $t \rightarrow \infty$ . In cases where the perturbation is assumed to be small ( $q_i \propto \epsilon$ ), neglecting the nonlinear (quadratic) terms in the equation allows for linear stability analysis. This involves examining the eigenvalues of the matrix  $A_{ij}$ . However, matrix  $A_{ij}$  might be non-normal, that is its eigenvectors might be non-orthogonal. Then perturbations might grow transiently reaching the amplitudes at which nonlinear terms cannot be neglected (Schmid 2007; Kerswell 2018).

An alternative method of stability analysis involves examining the derivative of the perturbation kinetic energy with respect to time. Assuming the kinetic energy of the perturbations is the inner product of the state vector

$$e = q_i q_i, \quad (2.2)$$

its temporal derivative can be easily obtained from (2.1)

$$\frac{de}{dt} = 2 A_{ij} q_i q_j + 2 Q_{ijk} q_i q_j q_k. \quad (2.3)$$

According to the Reynolds–Orr identity (Orr 1907; Schmid & Henningson 2001) (utilising Gauss divergence theorem), the nonlinear term does not influence the change in kinetic energy if the perturbations are confined by walls, are periodic or decay to zero in the far field, which are reasonable assumptions in most cases

$$2 Q_{ijk} q_i q_j q_k = 0. \quad (2.4)$$

From this point, matrices and vectors are denoted by bold letters to enhance readability. The Einstein summation notation is used when a three-dimensional array appears in an expression or the discussion.

The growth rate of the kinetic energy is

$$\mu_e = \frac{1}{e} \frac{de}{dt}, \quad (2.5)$$

and using (2.3) and (2.4) the following expression can be derived:

$$\mu_e = \frac{2 \mathbf{q}^T \mathbf{A} \mathbf{q}}{\mathbf{q}^T \mathbf{q}}. \quad (2.6)$$

The zero solution of (2.1) is Lyapunov stable if  $\mu_e < 0$  for any  $q_i$ . This statement is equivalent to ensuring that the maximum over any possible state is negative

$$\mu_{m,e} = \max_{\mathbf{q}} \mu_e(\mathbf{q}) < 0. \quad (2.7)$$

The numerator in (2.6) can be written as  $2 \mathbf{q}^T \mathbf{A} \mathbf{q} = \mathbf{q}^T (\mathbf{A} + \mathbf{A}^T) \mathbf{q}$ . Moreover, expression (2.6) represents the Rayleigh quotient of  $\mathbf{A} + \mathbf{A}^T$ . As  $\mathbf{A} + \mathbf{A}^T$  is symmetric,

the largest Rayleigh quotient corresponds to its largest eigenvalue, which is the maximum possible growth rate of kinetic energy

$$\max_{\mathbf{q}} \mu_e(\mathbf{q}) = \lambda_{\max}(\mathbf{A} + \mathbf{A}^T). \quad (2.8)$$

Therefore, the laminar state is Lyapunov stable if

$$\lambda_{\max}(\mathbf{A} + \mathbf{A}^T) < 0. \quad (2.9)$$

The critical state, which maximises the growth rate of kinetic energy, is the corresponding eigenvector. Unfortunately, this condition is sufficient but often far from necessary in practice. This analysis is referred to as energy method or nonlinear stability analysis since the results are valid for the nonlinear system due to the nonlinear terms not being assumed zero during the derivation but were eliminated by the Reynolds–Orr identity.

In many fluid dynamics applications, the primary concern is not just whether the flow is stable, but the critical limit at which instability arises. Notably, viscosity or the Reynolds number affects only the linear terms. In certain flow configurations, such as Poiseuille or Couette flows, the non-dimensionalised base flow is independent of viscosity, and the matrix  $\mathbf{A}$  can be decomposed into components that depend on the Reynolds number and those that do not

$$\mathbf{A}(Re) = \mathbf{A}_U + \frac{1}{Re} \mathbf{A}_R. \quad (2.10)$$

Considering that the Laplacian term can only dissipate kinetic energy,  $\mathbf{A}_R$  is a negative definite matrix. The smallest Reynolds number, for which  $\mu_{m,e} = 0$  and  $e \neq 0$ , is equal to the smallest Reynolds number, for which  $\mu_e$  can be 0, therefore it is equal to the smallest Reynolds number for which  $\mu_e = 0$ . By substituting (2.10) into (2.6), setting the expression to zero, and subsequently expressing  $Re$  and calculating its minimum through variation, we arrive at the corresponding Euler–Lagrange equation

$$(\mathbf{A}_R + \mathbf{A}_U^T) \mathbf{q} = \tilde{Re} (-\mathbf{A}_U - \mathbf{A}_U^T) \mathbf{q}. \quad (2.11)$$

This equation represents a general eigenvalue problem where the eigenvalue is the Reynolds number. The smallest eigenvalue, typically denoted as  $Re_E$ , is referred to as the global stability limit. If  $Re < Re_E$ , then  $\mu_{m,e} < 0$ , signifying unconditional stability.

## 2.2. The generalised kinetic energy method

The classical energy method often proves to be highly conservative, predicting Reynolds number limits below experimental observations. This issue arises because, at high Reynolds numbers, the  $\mathbf{A}$  matrix becomes non-normal. In such cases, the eigenvectors are non-orthogonal, and the energy of solutions initialised close to a linearly stable laminar state can grow significantly (Schmid 2007), although they do not necessarily transition to another state. Nerli *et al.* (2007) defined  $\mathbf{P}$  in a perturbed form, which is less general than the transformation matrix formulation presented in this work.

A possible way to define a generalised kinetic energy,  $h$ , is through the linear transformation of the variables by an invertible  $\mathbf{S}$  matrix

$$\mathbf{q} = \mathbf{S} \mathbf{r}, \quad (2.12)$$

and

$$h = \mathbf{r}^T \mathbf{r}. \quad (2.13)$$

The  $h$  function is the most general one among quadratic energy functions. Olivier Dauchot & Paul Manneville (1997) defined similarly the ‘exotic’ energy in their paper, where the transformation matrix is the eigenvectors of the linear part of the dynamical system. However, it is not optimal in general, a point that will be discussed later. In another form,  $h$  can be expressed as

$$h = \mathbf{q}^T \mathbf{P} \mathbf{q}, \quad (2.14)$$

where

$$\mathbf{P} = \mathbf{S}^{-T} \mathbf{S}^{-1}, \quad (2.15)$$

and the matrix  $\mathbf{P}$  is clearly positive definite.

Among quadratic energy functions, there is no way to improve the global stability results obtained with kinetic energy (Goulart & Chernyshenko 2012), therefore  $h$  is constructed to prove the conditional stability of the laminar state. A conditional Lyapunov function must meet the following requirements:

$$h(\mathbf{q}) > 0 \text{ if } \mathbf{q} \neq \mathbf{0} \text{ and } h(\mathbf{q}) = 0 \text{ if } \mathbf{q} = \mathbf{0}, \quad (2.16)$$

and

$$\frac{\partial h}{\partial q_i} \frac{dq_i}{dt} < 0 \text{ if } h(\mathbf{q}) < \gamma_a^2. \quad (2.17)$$

The region where  $h(\mathbf{q}) < \gamma_a^2$  represents the provable region of attraction (ROA) of the origin, although the true ROA can be larger in general. The definition of  $h$  in (2.14) automatically satisfies the first condition (2.16). Our objective is to maximise the size of the ROA satisfying equation (2.17) by constructing an optimal  $h$  function. Here, the smallest radius,  $\sqrt{e_{min}}$  in the original state space is used to describe the region since it makes the results of minimal seed calculations comparable.

There are three essential parts of the investigation. The first is verifying that a given  $h$  satisfies equation (2.17). The second involves maximising the ROA and  $\gamma_a$  for a given  $h$ , where the critical value  $\gamma_{crit}$  determines  $\sqrt{e_{min}}$ . The third focuses on finding the optimal  $h$  that maximises this region.

### 2.2.1. Validating the generalised kinetic energy to be a conditional Lyapunov function

For the validation of (2.17), it is convenient to transform the differential equation (2.1) for the new variables

$$\frac{dr_i}{dt} = S_{ij}^{-1} A_{jk} S_{kl} r_l + S_{ij}^{-1} Q_{jkl} S_{km} r_m S_{lo} r_o. \quad (2.18)$$

To facilitate this transformation, let us define

$$\tilde{A}_{ij} = S_{il}^{-1} A_{lk} S_{kj}, \quad (2.19)$$

$$\tilde{Q}_{ijk} = S_{im}^{-1} Q_{mol} S_{oj} S_{lk}. \quad (2.20)$$

These transformations result in a similar ordinary differential to (2.1), if  $A_{ij}$  and  $Q_{ijk}$  are replaced by  $\tilde{A}_{ij}$  and  $\tilde{Q}_{ijk}$ , respectively.

To analyse the system at different perturbation levels, the perturbation magnitude  $\gamma$  is introduced by decomposing the transformed state vector into its magnitude,  $\gamma = \sqrt{r_i r_i}$ , and a unit vector

$$r_i = \gamma \tilde{r}_i. \quad (2.21)$$

Next, let us define the growth rate of the generalised kinetic energy

$$\mu_h = \frac{1}{h} \frac{dh}{dt}, \quad (2.22)$$

which can be calculated as

$$\mu_h = \frac{2 \tilde{A}_{ij} r_i r_j + 2 \tilde{Q}_{ijk} r_i r_j r_k}{r_l r_l} = 2 \tilde{A}_{ij} \tilde{r}_i \tilde{r}_j + 2 \gamma \tilde{Q}_{ijk} \tilde{r}_i \tilde{r}_j \tilde{r}_k. \quad (2.23)$$

The main difference lies in the quadratic term ( $\tilde{Q}_{ijk}$ ) contributing to the growth rate of the generalised kinetic energy ( $h$ ), unlike in the case of the original kinetic energy ( $e$ ). Due to the presence of this term, only conditional but not unconditional stability can be established, and it can be utilised to calculate the threshold amplitude ( $\gamma_{crit}$ ).

Let us define the possible maximum growth rate at a given level of perturbation as

$$\mu_{max,h}(\mathbf{S}, \gamma) = \max_{\tilde{\mathbf{r}}} \mu_h(\tilde{\mathbf{r}}, \mathbf{S}, \gamma). \quad (2.24)$$

The generalised kinetic energy,  $h$ , should first be investigated at zero perturbation level,  $\gamma = 0$ . There, similarly to the formula (2.8), the largest growth rate can be determined as

$$\mu_{h,lin,max} = \mu_{max,h}(\mathbf{S}, \gamma = 0) = \lambda_{max}(\tilde{\mathbf{A}} + \tilde{\mathbf{A}}^T), \quad (2.25)$$

where  $\lambda_{max}$  denotes the largest eigenvalue of a matrix. If  $\lambda_{max}(\tilde{\mathbf{A}} + \tilde{\mathbf{A}}^T) \geq 0$ , then  $h$  cannot demonstrate the existence of a ROA, similar to how the original kinetic energy,  $e$ , fails to do so if  $Re > Re_E$ . However, it is well known that if the equilibrium point is linearly stable, a suitable  $h$  function must exist, ensuring the maximal generalised kinetic energy growth rate of the linearised system is negative. For instance, the eigenvectors of  $\mathbf{A}$  can be used to construct such a function.

If  $\lambda_{max}(\tilde{\mathbf{A}} + \tilde{\mathbf{A}}^T) < 0$ ,  $h$  can prove the existence of a ROA. The next step is to increase  $\gamma$  and expand the ROA until the point where the maximal growth becomes zero, ( $\gamma = \gamma_{crit}$ ). Since the growth rate must not exceed the maximum growth rate, and the maximum remains negative up to this perturbation level, the generalised kinetic energy or  $h$  decreases monotonically, if  $\gamma < \gamma_{crit}$ . Therefore, the second requirement (2.17) of the conditional Lyapunov function is fulfilled.

Finding the global maximum of the growth rate at a given perturbation level among the various states ( $\mathbf{r}$ ) is essential for proving that  $h$  is a conditional Lyapunov function. This will be achieved using robust optimisation techniques, initialised from multiple seed points to increase the likelihood of accurately identifying the global maximum. Unfortunately, the optimisation procedure was not discussed in the paper by Nerli *et al.* (2007), and thus this aspect of the present study fills an important gap in validating the method.

### 2.2.2. Calculation of the maximal growth of the generalised kinetic energy

Proving that a specific  $\tilde{\mathbf{r}}$  maximises the expression in (2.23), while also adhering to the constraint that ( $\|\tilde{\mathbf{r}}\| = 1$ ), presents a formidable challenge.

Analytical form of (2.23) helps to derive the gradient and the Hessian, accelerating the optimisation. Among the various methods explored are sequential quadratic programming (SQP), the active set algorithm and the interior-point algorithm (Nocedal & Wright 2006), all of which can be efficiently employed using MATLAB's *fmincon* function.

First, various dynamical models with increasing degrees of freedom,  $n$ , are generated. For  $n = 2$ , the TTRD' model is utilised, for  $n = 4$  the W95A (defined in § 3.1) model is employed, and for  $n = 12, 18, 24, 30, 45, 60, 90, 150$ , a range of Poiseuille flow models (PFMs) are considered. The specifics of these models will be detailed later.

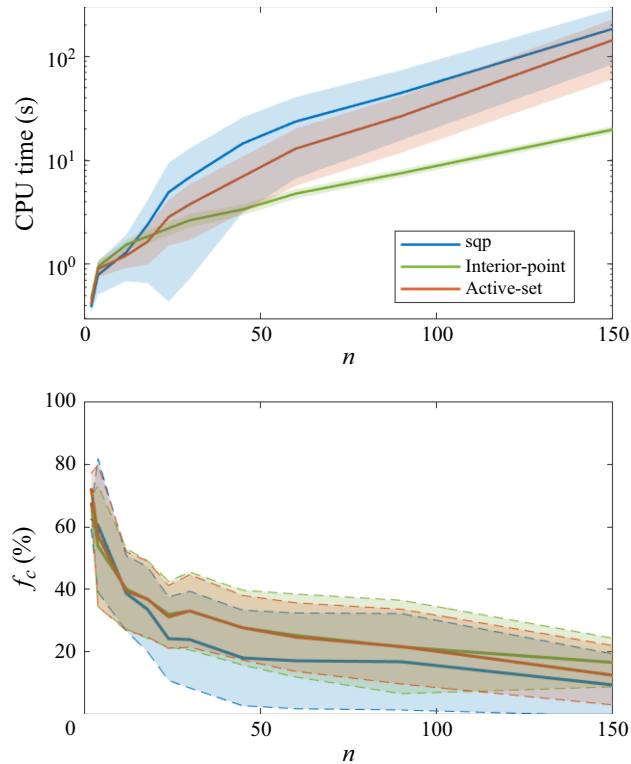


Figure 1. Computation time for calculating the maximal growth rate (a) and the relative frequency of solutions achieving the actual maximum (b) as functions of the dynamical system's degrees of freedom. The shaded areas represent the standard deviation from the mean values.

The optimisation process was conducted for each dynamical model using 20 randomly generated transformation matrices, across a spectrum of relatively high perturbation levels  $\gamma = 0.1, 0.2, 0.5, 1, 2, 5, 10$ . For each model, 100 randomly generated seed points – unitary  $\tilde{\mathbf{r}}$  state vectors – were created. From each seed point, optimisation was executed using three distinct algorithms. The global maximum for a given transformation matrix at a specified perturbation level was determined as the maximum across all optimisation techniques and seed points. The methods were compared based on the convergence rate, defined as the proportion of solutions that converged to the global maximum from differently initialised optimisations.

The convergence rate as a function of the number of degrees of freedom is depicted in figure 1(b), with the thick curve representing the mean value and the dashed line and shadow indicating the standard deviation of the convergence rate across various perturbation levels and transformation matrices. For systems with few degrees of freedom, the convergence rate was approximately 70 %, decreasing to 20 % as  $n$  increases. For small systems ( $n < 20$ ), no significant difference was observed among the optimisation algorithms; however, for larger systems ( $n > 100$ ), the interior-point algorithm clearly outperformed the others. Its mean convergence rate was higher, and its standard deviation was smaller. Although not visualised here, the convergence rate as a function of perturbation level was evaluated. For SQP and active set methods, the convergence rate decreased with increasing perturbation level, whereas for the interior-point algorithm, it remained nearly constant. Based on the convergence rate, the interior-point algorithm is superior, especially for large dynamical systems.

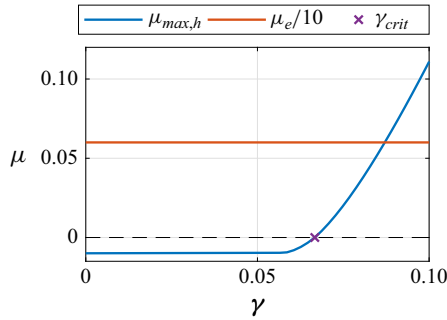


Figure 2. The maximal growth rate of the generalised kinetic energy ( $\mu_{max,h}$ ) as the function perturbation magnitude  $\gamma$  in the case of the optimally transformed TTRD' model at  $Re = 5$ . The red curve represents the one tenth of the growth rate of the original kinetic energy ( $\mu_e = 0.6$ ), which is independent of the perturbation level.

Computational time comparison, shown in figure 1(a), reveals that, for smaller systems ( $n < 12$ ), the SQP method is the fastest. There exists a narrow range ( $12 < n < 20$ ) where the active set method is optimal. For larger systems, the interior-point method is significantly faster than the other two methods, primarily because it utilises the analytical Hessian matrix, unlike the other methods.

In summary, the SQP method is recommended for small systems, while the interior-point method is better suited for larger ones. To determine the maximum growth rate for a given transformation matrix and perturbation level, optimisation is repeated from random initial points until at least five solutions converge to the same maximum value, reducing the risk of converging to a local maximum.

Since finding the global maximum is critical, the interior-point method's convergence rate was analysed for dynamical models with up to 330 degrees of freedom. At this scale, the convergence rate drops to 5.81%. Assuming a sufficiently large sample, this rate can approximate the probability of locating the global maximum with a random initial guess. With 231 random initial guesses, the probability of missing the global maximum decreases to 1 in  $10^6$ , making failures highly unlikely. The applied rule requiring at least five consistent results often necessitates even more initial guesses.

### 2.2.3. Calculation of the critical perturbation level

As the  $\mu_{max,h}$  function is created by a proper optimisation procedure, the next step is to determine the largest possible critical perturbation level below which this growth is negative

$$\mu_{max,h}(\mathbf{S}, \gamma_{crit}) = 0. \quad (2.26)$$

The corresponding unitary state vector, defined by

$$\mu_{max,h}(\mathbf{S}, \gamma_{crit}) = \mu_h(\tilde{\mathbf{r}}_{crit}, \mathbf{S}, \gamma_{crit}), \quad (2.27)$$

can be utilised to obtain the critical state:  $\mathbf{r}_{crit} = \gamma_{crit} \tilde{\mathbf{r}}_{crit}$ .

For illustration,  $\mu_{max,h}$  is plotted in figure 2 for one particular problem. At low  $\gamma$  values, the linear part of the dynamical system dominates, where the maximum growth rate is almost constant and equal to the Rayleigh quotient of the  $\tilde{A}_{ij} + \tilde{A}_{ji}$  matrix, see equation (2.25). For higher  $\gamma$  values, the nonlinearity of the system influences the maximal growth, which tends towards a straight line. The slope of this line corresponds to the maximum of  $\{2 \tilde{Q}_{ijk} \tilde{r}_i \tilde{r}_j \tilde{r}_k\}$  among possible  $\tilde{r}_i$  states. Figure 2 illustrates the maximal growth rate of the original kinetic energy, highlighting that the laminar state is unstable according to the

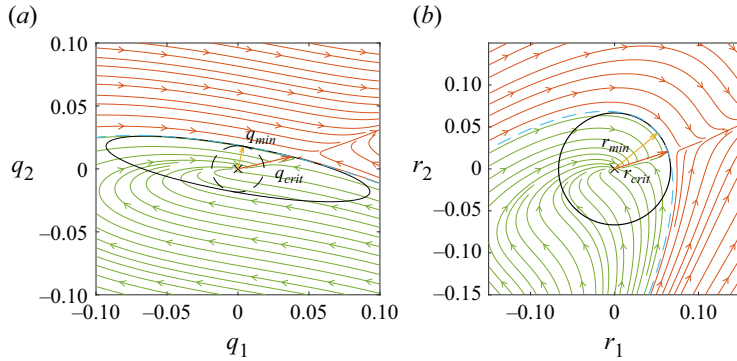


Figure 3. The phase space trajectories of the TTRD' model at  $Re = 5$  are shown for the original state variables (a) and for the optimally transformed variables (b). Green trajectories converge towards the origin, while red trajectories tend to another equilibrium point, which is not shown. The black curve represents the provable boundary of the ROA utilising the optimal  $h$  function. The dashed, blue curve shows the boundary of the true ROA. The red vector is the critical perturbation (2.26), where the growth rate of the generalised kinetic energy was zero at the critical perturbation level (2.27). The yellow vector illustrates the smallest perturbation (2.30) in the original state space (a) whose length is equal to the critical perturbation in the optimally transformed state space (b).

regular energy method. Moreover, it demonstrates that the original kinetic energy remains constant and is unaffected by the perturbation amplitude.

Determining the critical perturbation level is relatively simpler compared with the other parts of the method. It involves finding the roots of equation (2.26). The gradient of this expression can be derived easily as

$$\frac{\partial \mu_{max,h}}{\partial \gamma} = 2 \tilde{Q}_{ijk} \tilde{r}_{max,i} \tilde{r}_{max,j} \tilde{r}_{max,k} \quad (2.28)$$

where  $\tilde{r}_{max}$  is the vector that maximises the growth rate at a given perturbation level. By leveraging the analytical gradient, the Newton method, renowned for its second-order convergence rate, is utilised effectively. Typically, after a few iterations (5–6), the solution's residual falls below the tolerated error threshold of  $10^{-10}$ .

The investigated region can be envisioned as a multidimensional hypersphere in the  $\mathbf{r}$  state space around the origin. The radius of this sphere is  $\gamma$ . If the radius is smaller than a critical value  $\gamma_{crit}$ , then  $\mu_h < 0$ , indicating that the generalised kinetic energy ( $h$ ) is decreasing, and the trajectories move inward, ultimately converging to the origin. At the critical radius, a trajectory becomes tangential to the sphere and may not reach the origin. The hypersphere with radius  $\gamma_{crit}$  represents the boundary of the provable ROA. However, states outside this sphere can belong to the basin of attraction of either the origin or another attractor. In the case of the two-dimensional problem, the hyperspherical ROA reduces to a circle and is illustrated in figure 3(b) in the case of an optimal transformation matrix and  $h$  function.

It is more interpretable to transform the ROA back to the original state space. The linear transformation (scaling and rotating) of the hypersphere results in a hyperellipsoid in the original state space  $\mathbf{q}$ . This hyperellipsoid defines the boundary of the provable ROA of the origin. A standard quantity describing ROA is its smallest radius,  $\sqrt{e_{min}}$ .

The value  $e_{min}$  can be calculated using equations (2.2) and (2.21) as follows:

$$e_{min}(\mathbf{S}) = \gamma_{crit}^2(\mathbf{S}) \min_{\tilde{\mathbf{r}}} \{ \tilde{\mathbf{r}}^T \mathbf{S}^T \mathbf{S} \tilde{\mathbf{r}} \}. \quad (2.29)$$

The argument of the minimum function is the Rayleigh quotient of  $\mathbf{S}^T \mathbf{S}$ , and the minimum value corresponds to the smallest eigenvalue of  $\mathbf{S}^T \mathbf{S}$ , since  $\mathbf{S}^T \mathbf{S}$  is a symmetric matrix

$$e_{min}(\mathbf{S}) = \gamma_{crit}^2(\mathbf{S}) \lambda_{min}(\mathbf{S}^T \mathbf{S}). \quad (2.30)$$

The corresponding unitary eigenvector  $\tilde{\mathbf{r}}_{min}$  can be utilised to get the two locations  $\mathbf{q}_{min} = \pm \gamma_{crit} \mathbf{S} \tilde{\mathbf{r}}_{min} = \pm \mathbf{S} \mathbf{r}_{min}$ , where the inner hypersphere touches the hyperellipsoid, as illustrated in figure 3(a). This inner hypersphere is a subset of the provable ROA, where  $e < e_{min}$ .

The value of  $e_{min}$  depends on the definition of  $h$  through the transformation matrix  $\mathbf{S}$ . The aim of the method is to maximise this minimum energy,  $e_{min}(\mathbf{S})$  over all matrices,  $\mathbf{S}$ . The possible methods for maximisation will be discussed in § 2.3. It is important to note that the value of  $\gamma$  is only meaningful for a specific transformation or generalised kinetic energy. Comparisons of  $\gamma$  or  $\gamma_{crit}$  between different  $\mathbf{S}$  matrices or  $h$  functions are not valid.

It should also be mentioned that although the kinetic energy ( $e$ ) can grow significantly inside the provable ROA region – a phenomenon usually called the non-modal growth – stability is guaranteed there due to the exponential decay of  $h$  there.

### 2.3. Optimising the generalised kinetic energy

The last key question is how to determine the optimal  $h$  function, represented by the transformation matrix  $\mathbf{S}_{opt}$ , to maximise the size of the provable ROA,  $e_{min}$ . First, a method utilising the singular value decomposition (SVD) of the eigenvectors is presented. This method cannot provide the largest  $e_{min}$ , but it is extremely fast compared with other methods. As a second approach, all the elements of the transformation matrix are treated as decision variables, leading to a significantly larger ROA at the cost of higher computational need.

#### 2.3.1. The GKE-SV method utilising the singular value decomposition of the eigenvector matrix

A plausible starting point is to use the eigenvectors of  $\mathbf{A}$ ,  $\Psi_c$ , as the transformation matrix, since it diagonalises the  $\mathbf{A}$  matrix. This transformation redefines the state variables as coefficients of the eigenmodes, addressing non-normality by making  $\tilde{\mathbf{A}}$  diagonal and its eigenvectors orthogonal. Consequently, the GKE, expressed as the sum of squared eigenmode coefficients, ensures stability at infinitesimally low perturbation levels, as noted by Olivier Dauchot & Paul Manneville (1997).

Diagonalising  $\mathbf{A}$  with  $\Psi_c$  results in the maximum linear growth rate of

$$\mu_{h,lin,max}(\Psi_c) = \lambda_{max}(\tilde{\mathbf{A}} + \tilde{\mathbf{A}}^T) = 2Re(\lambda_{max}(\mathbf{A})), \quad (2.31)$$

which must be negative if the equilibrium point is linearly stable and there exists a certain provable ROA. However, it will be shown that  $\Psi_c$  used to define  $h$  is not optimal, but systematic modifications can yield an improved transformation matrix and  $h$ .

As a first step, the eigenvector matrix is transformed into a real-valued matrix, denoted as  $\Psi$ . This involves reinterpreting all eigenvector pairs associated with the same complex-conjugate eigenvalue pairs, alternately focusing on the real and imaginary components, and subsequently normalising these to unit vectors. Although this new transformation matrix does not diagonalise the  $\mathbf{A}$  matrix, the formulation of generalised energy remains analogous and equation (2.31) still holds.

Next, the SVD of  $\Psi$  matrix is performed

$$\Psi = \mathbf{U}_{\psi} \mathbf{S}_{\psi} \mathbf{V}_{\psi}. \quad (2.32)$$

It can be demonstrated that  $\mathbf{V}_{\psi}$  does not affect the definition of  $h$  in equation (2.15) and  $\mathbf{V}_{\psi}$  can therefore be omitted.

For simplicity, the singular values can be normalised by their maximum without sacrificing generality. Furthermore, let the singular values be denoted by  $s_i$ , where  $s_1$  is the largest and  $s_n$  is the smallest. Due to normalisation  $s_1 = 1$  and  $0 < s_i \leq 1$ . It is well known that, as the Reynolds number increases, the non-normality of  $\mathbf{A}$  or the condition number of the eigenvector matrix increases. Therefore, the smallest singular value of  $\Psi$ ,  $s_n$ , tends toward zero, leading to two significant issues. One problem is that a decreasing  $s_n$  makes the eigenvector matrix ill conditioned and difficult to invert accurately. Additionally, this choice likely reduces the size of ROA,  $e_{min}$ , since

$$e_{min} \propto \lambda_{min}(\mathbf{S}^T \mathbf{S}) = s_n^2, \quad (2.33)$$

according to equation (2.30). Visually, utilising  $\Psi$  as the transformation matrix results in an attraction region shaped like a narrow superellipsoid with its smallest axis shrinking to zero. In this context, the concept of ‘exotic’ energy as defined by Olivier Dauchot & Paul Manneville (1997), while effective for two-dimensional systems at lower Reynolds numbers, is presumably inefficient for larger systems or those at higher Reynolds numbers, where the ratio of the smallest and largest singular values of  $\Psi$  becomes large.

A straightforward solution to the problem is proposed by modifying the transformation matrix as

$$\mathbf{S} = \mathbf{U}_{\psi} \tilde{\mathbf{S}}_{\psi}, \quad (2.34)$$

where  $\mathbf{U}_{\psi}$  comes from the SVD decomposition of  $\Psi$  and  $\tilde{\mathbf{S}}$  is the modified matrix of the singular values ( $\mathbf{S}_{\psi}$ ), for which the singular values smaller than a certain threshold,  $s_{min}$ , are simply set to  $s_{min}$

$$\tilde{s}_i = \begin{cases} s_i & \text{if } s_i > s_{min}, \\ s_{min} & \text{if } s_i \leq s_{min}. \end{cases} \quad (2.35)$$

The threshold parameter,  $s_{min}$ , can be set between  $s_n$  and 1. If  $s_{min} = s_n$ , the transformation matrix is equivalent to the eigenvector matrix in terms of the  $h$  definition. Conversely, if  $s_{min}$  is set to 1, the transformation has no effect, making the GKE equivalent to  $e$ . In this case, if  $Re > Re_E$ , no provable ROA exists according to  $h$ .

By varying  $s_{min}$ , between the two extrema,  $\mu_{h,lin,max}$  increases continuously and changes sign. This behaviour is illustrated in figure 4, which shows the maximal growth rate of the linearised system rate after transformation as a function of  $s_{min}$  for the  $n = 210$  PFM at  $Re = 2000$ . Interestingly, for various systems,  $s_{min}$  can be increased by orders of magnitude above the smallest original singular values without significantly affecting  $\mu_{h,lin,max}$ . In the presented case,  $s_{min}$  is increased by two orders of magnitude without altering  $\mu_{h,lin,max}$ . This demonstrates that the non-normality of  $\mathbf{A}$  can be effectively managed without relying on an ill-conditioned transformation matrix. Moreover, increasing  $s_{min}$  significantly enlarges the provable ROA, as  $\sqrt{e_{min}}$  is proportional to the smallest singular value of the transformation matrix.

During the optimisation of the transformation matrix, the optimal  $s_{min}$  is determined using a bisection algorithm. The algorithm increases  $s_n$  with a relative accuracy of  $10^{-3}$  until  $\mu_{h,lin,max}$  no longer exceeds a relative change of  $10^{-5}$  from its minimum possible value.

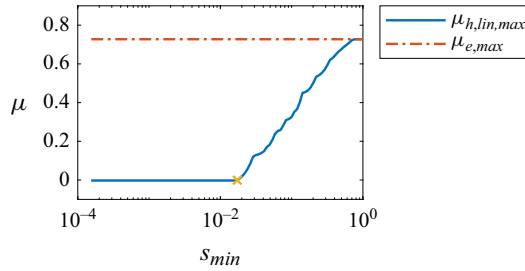


Figure 4. The maximal growth rate of the GKE ( $\mu_{h,lin,max}$ ) for the linearised system, plotted against the smallest singular value of the modified eigenvector matrix at  $Re = 2000$ . The system in question is the 210-dimensional PFM. The red curve depicts the maximal growth rate of the original kinetic energy, while the yellow cross marks the critical  $s_{min}$  value at which the growth rate becomes zero.

The optimisation of  $\mathbf{S}$  such a way offers both benefits and limitations due to its disregard for nonlinear terms. This exclusion streamlines the optimisation, significantly speeding up the process as it necessitates only the eigenvalue analysis of relatively small matrices. After optimising the transformation matrix, a solitary evaluation is sufficient for computing the ROA. However, this method may not achieve optimality, given that it neglects the impact of nonlinear terms during the optimisation of the transformation matrix. This approach has been named the ‘GKE-SV’ algorithm in the context of this study.

### 2.3.2. The GKE-G method – general optimisation of the transformation matrix

An alternative approach involves optimising the elements of the transformation matrix as decision variables to maximise the size of the provable ROA,  $e_{min}$  value. Given that only the definition of  $h$  ( $\mathbf{P}$  in equation (2.15)) affects the stability analysis, we can assume, without loss of generality, that  $\mathbf{S}$  is an upper triangular matrix. This assumption reduces the number of unknowns from  $n^2$  to  $(n^2 + n)/2$ . As the degrees of freedom expand, the number of decision variables increases quadratically, necessitating gradient-based optimisation. The derivation of the gradient is elaborated in [Appendix A.2](#).

This approach to optimising the transformation matrix is comprehensive, allowing for the identification of the optimum among all possible quadratic Lyapunov functions. Despite this advantage, the method requires multiple evaluations of the ROA, making it computationally intensive. Even with the utilisation of gradients with respect to decision variables to expedite the process, the computational demands remain significant. To manage the complexity and the high number of unknowns efficiently, the interior-point algorithm is employed in this study.

The general optimisation procedure for  $\mathbf{S}$  unfolds as follows:

- (i) Solve (2.26) to determine  $\gamma_{crit}$ .
- (ii) Calculate  $e_{min}$  through (2.30).
- (iii) Update  $\mathbf{S}$  through the interior-point algorithm, guided by the gradient (A9), and iteratively repeat the first two steps until  $e_{min}$  (2.30) reaches its maximum value.

This methodical enhancement of  $\mathbf{S}$  ensures that the optimisation steadily moves towards a maximum of  $e_{min}$ , which can of course be only local rather than global. In the paper, this optimisation procedure of the transformation matrix is referred to as the ‘GKE-G’ algorithm.

#### 2.4. Comparison of the generalised kinetic energy method and sum-of-squares programs

This section introduces a comparison between the proposed procedure for constructing Lyapunov functions and the current state-of-the-art methodologies, particularly those employing SOS programs. A brief description of the applied SOS methods is provided in [Appendices A.2.1](#) and [A.2.2](#).

The first SOS program, SOS1 (Jarvis-Wloszek 2003; Tan & Packard 2008; Topcu *et al.* 2008; Khodadadi *et al.* 2014; Kalur *et al.* 2021), consists of three SOS constraints, one ensures the positive definiteness of the Lyapunov function, the second maximises the size of the ROA while the third mandates that the Lyapunov function decreases along the solution trajectories. The maximal ROA can be obtained by an iterative maximisation of the parameters of the constraints.

The second SOS program, SOS2 (Liu & Gayme 2020), is similar to the SOS1 program but the second constraint is replaced by an eigenvalue problem, significantly reducing the size of the problem and the necessary number of iterations. Therefore, SOS2 is usually faster but less accurate compared with the SOS1 method.

There is a convex formulation, SOS3, for inner approximating a basin of attraction introduced by Henrion & Korda (2014) which avoids the necessary iteration steps of the SOS1 and SOS2 programs. However, in SOS3, time appears as an explicit variable in the polynomials, unlike in SOS1 and SOS2. Additionally, SOS3 consist of four SOS constraints, resulting in significantly larger optimisation problem. Furthermore, it requires the explicit specification of a time horizon and a target domain. These parameters play a critical role in shaping the results. This formulation is excluded from the comparison.

The two SOS algorithms and the two GKE algorithms were evaluated against each other using simple models, focusing on computational time and the size of the ROA as key metrics. For the conversion of SOS programs into a semi-definite program (SDP), two tools, SOSTOOLS (Papachristodoulou *et al.* 2013) and Yalmip (Löfberg 2004), were employed. However, no significant difference in computational time was observed between them. Consequently, the results presented here utilise the conversion code provided by SOSTOOLS, with the SDP problems solved using MOSEK.

The ROA was calculated for five dynamical systems: TTRD', W95A, W95B, BT and PFM<sub>*n*=12</sub>. These systems have degrees of freedom (*n*) of 2, 4, 4, 4 and 12 respectively. Here, PFM<sub>*n*=12</sub> denotes the truncated Galerkin model of Poiseuille flow, while the other models are low-order representations of subcritical transition. These calculations were performed on a computer equipped with an Intel i7-7700 processor running at 3.6 GHz and 32 GB of memory with a speed of 2400 MHz.

The comparative analysis in [figure 5](#) illustrates the performance differences between the GKE and SOS algorithms in determining the ROA for dynamical systems. The GKE-G algorithm identified a ROA radius identical to that of the SOS1 method for low-dimensional models ( $n \leq 4$ ) and slightly smaller for the  $n = 12$  model, but required more time to do so. The small difference is attributed to the optimisation of the  $h$  function in the GKE-G method. When the optimal  $h$  definition obtained by the SOS1 algorithm was used to calculate the provable ROA using the GKE-G method, the radius matched that of the SOS1 method. The SOS2 algorithm yielded a slightly smaller ROA, whereas the GKE-SV algorithm predicted significantly smaller regions but demanded substantially less computational resources.

For smaller systems, the SOS1 algorithm is recommended due to its precision. The increased computational demand typically does not pose a significant concern for these cases. However, it has been discovered that the SOS1 method becomes impractical for systems with more than 15 degrees of freedom, as the resultant SDP becomes too large for

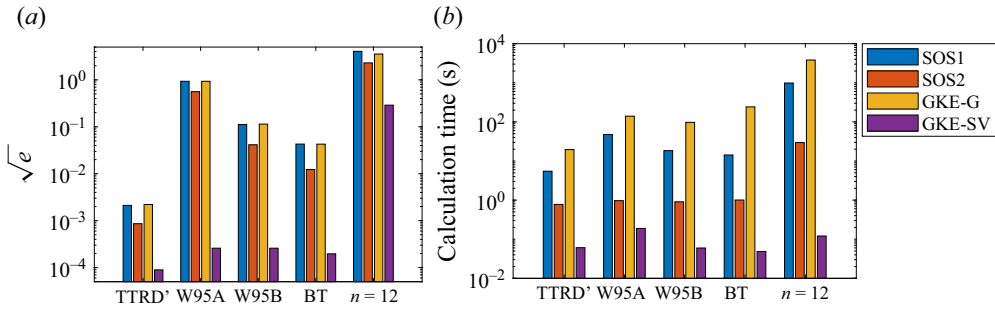


Figure 5. Threshold amplitude (a) across five dynamical systems (TTRD', W95A, W95B, BT, PFM<sub>n=12</sub>) at a Reynolds number of  $Re = 5Re_E$ , as determined by four distinct methods, alongside the computational time (b).

the optimisation program, MOSEK, to solve. Similar limitations were observed with the SOS2 algorithm when the degrees of freedom exceeded 21.

A core issue identified is that, even when restricting the analysis to quadratic Lyapunov functions, the left-hand side of equations (A18–A19) in SOS1 and (A22) in SOS2 manifest as fourth-order polynomials. To ascertain their positive definiteness, the necessary number of monomials is proportional to  $n^2$ , implying that the optimisation matrix size – containing the decision variables – scales roughly with  $n^4$ . Consequently, the number of decision variables surges as the degrees of freedom ( $n$ ) increase. The SOS2 algorithm accommodates slightly larger systems due to involving only one fourth-order polynomial, in contrast to the two present in SOS1.

Conversely, GKE methods exhibit scalability to systems an order of magnitude larger, as will be demonstrated. Notably, the GKE-G method provides an approximation of the ROA comparable in accuracy to the widely utilised SOS1 method, offering a viable alternative for larger system analysis. The GKE method exemplifies a less conservative approach with better scalability.

### 3. Application

#### 3.1. Trefethen's and Waleffe's models

Well-known low-order dynamical systems that mimic the subcritical transition of shear flows are investigated in this study. Specifically, the two-dimensional TTRD' model of Baggett & Trefethen (1997) and the four-dimensional W95 model of Waleffe (1995) are examined. In these models, the linearised part (**A**) is non-normal, and the condition number of its eigenvector matrix grows with increasing Reynolds number. Meanwhile, the nonlinear part does not affect the growth rate of kinetic energy, as the corresponding matrix remains asymmetric.

The TTRD' model is represented by the following equation:

$$\frac{d\mathbf{q}}{dt} = \begin{bmatrix} -\frac{1}{Re} & 1 \\ 0 & -\frac{1}{Re} \end{bmatrix} \mathbf{q} + \begin{bmatrix} 0 & -q_1 \\ q_1 & 0 \end{bmatrix} \mathbf{q}, \quad (3.1)$$

therefore the non-zero elements of  $Q_{ijk}$  are

$$Q_{112} = -1, \quad (3.2)$$

$$Q_{211} = 1. \quad (3.3)$$

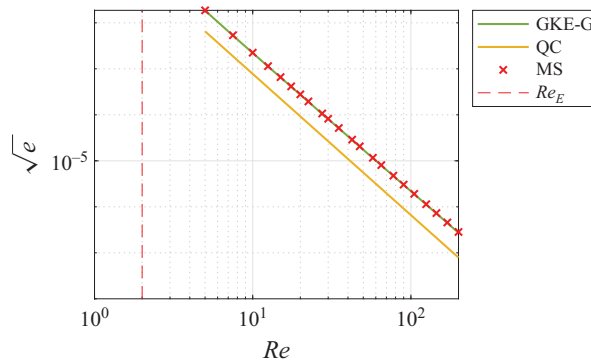


Figure 6. The size of ROA as the function of Reynolds number in the case of TTRD' model. The fitted curve from Liu & Gayme (2020) using the QC method ( $0.912 Re^{-3.07}$ ) is shown alongside. The best-fitting curve of GKE-G results is  $\sqrt{e_{min}} \approx 2.228 Re^{-3.005}$ . The red crosses represent the energy of the approximated minimal seeds. The vertical red line signifies the unconditional stability limit  $Re_E = 2$ .

The optimal  $h$  functions and the corresponding transformation matrices for TTRD', that maximise  $e_{min}$ , are calculated at the Reynolds number between 5 and 100 with the step size 2.5 by the proposed GKE-G method. The result is visualised in figure 3 at  $Re = 5$ , where green trajectories converge to the origin and red trajectories to another state. These trajectories are shown in the original variables (figure 3a) and the transformed variables (figure 3b). The calculated ROA appears as an ellipse in the original state space, precisely touching the boundary of the true ROA.

Next, the calculated threshold amplitude as the function of Reynolds number are plotted in figure 6 and compared with the findings of Liu & Gayme (2020). The cited authors used the quadratic constraint method, which has been proven to be computationally efficient. They treated the nonlinear term as a forcing with an approximated upper bound.

The calculated threshold amplitude ( $\sqrt{e_{min}}$ ) decays as a function of the Reynolds number following a power law. The exponents are nearly identical:  $-3.005$  in this study and  $-3.07$  in the work of Liu & Gayme (2020). However, the method presented here predicts a ROA with a radius roughly three times larger, indicating a energy level approximately one magnitude higher. This substantial difference arises from their approximation of the nonlinear term, while GKE-G calculation takes into account the exact terms, providing a more precise representation of the system's behaviour, similarly to SOS methods.

In the next step, the accuracy of the ROA is investigated by solving the ordinary differential equation initialised close to the outside of the calculated ROA. The solutions are initialised from slightly increased threshold state vectors  $\mathbf{q}_0 = c_u \mathbf{q}_{min}$  approximating the minimal seed states and computed using the Matlab *ode45* Runge–Kutta method.

The average value of  $c_u$  for such solutions is found to be 1.02, indicating that the proposed method is highly accurate for this small model. The energy level of these approximated minimal seeds are shown in figure 6 but they are almost on the curve representing the radius of ROA.

In the next step, the GKE-G method is applied to the low-order model of subcritical transition proposed by Waleffe (1995). The dynamical system is represented as follows:

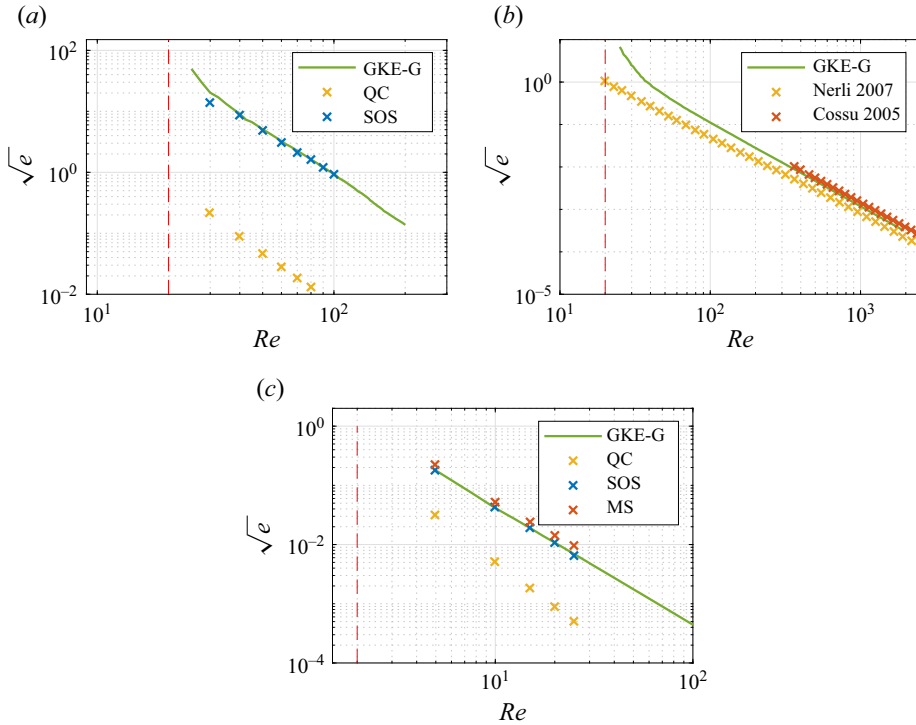


Figure 7. The size of the ROA as the function of the Reynolds number in the case of the W95A model (a), W95B model (b) and BT model (c), computed using the GKE-G method. The QC, SOS, MS curves represent the results of Kalur *et al.* (2021) and MS refers to minimal seeds obtained via direct-adjoint looping. For the W95B model, the minimal seed energy is taken from Cossu (2005). The red, vertical dashed line indicates the unconditional stability limit,  $Re_E$ . The best-fitting curves of  $\sqrt{e_{min}}$ :  $\sqrt{e_{min}} \approx 176479 Re^{-2.65089}$  for W95A;  $\sqrt{e_{min}} \approx 1964.3 Re^{-2.08506}$  for W95B;  $\sqrt{e_{min}} \approx 4.1952 Re^{-1.98875}$  for BT model.

$$\frac{d\mathbf{q}}{dt} = \frac{1}{Re} \begin{bmatrix} -\lambda_w & Re & 0 & 0 \\ 0 & -\mu_w & 0 & 0 \\ 0 & 0 & -\nu_w & 0 \\ 0 & 0 & 0 & -\sigma_w \end{bmatrix} \mathbf{q} + \begin{bmatrix} -\gamma_w q_3^2 + q_2 q_4 \\ \delta_w q_3^2 \\ \gamma_w q_3 q_1 - \delta_w q_3 q_2 \\ -q_4 q_2 \end{bmatrix}. \quad (3.4)$$

The parameters  $\lambda_w$ ,  $\mu_w$ ,  $\nu_w$ ,  $\sigma_w$  represent the decay rates due to viscosity, while  $\gamma_w$ ,  $\delta_w$  describe the nonlinear interaction between rolls ( $q_2$ ) and streaks ( $q_1$ ).

In this study, three different parameter sets are investigated. The first set is characterised by  $\lambda_w = \mu_w = \sigma_w = 10$ ,  $\nu_w = 15$ ,  $\delta_w = 1$ ,  $\gamma_w = 0.1$ , denoted as the W95A model (Waleffe 1995). The parameters of the second set remain the same except  $\gamma_w = 0.5$ , and this configuration is denoted as W95B. In the last case, all parameters are set to 1,  $\lambda_w = \mu_w = \nu_w = \sigma_w = \delta_w = 1$ , and this configuration is denoted as the BT model (Baggett & Trefethen 1997). It is important to note that these parameter sets significantly influence the system dynamics (Baggett & Trefethen 1997; Kalur *et al.* 2021).

The optimised transformation matrices are calculated for the W95A, W95B and BT models over different ranges of Reynolds numbers: 25–200 for the W95A model, 25–2000 for the W95B model and 5–100 for the BT model by the GKE-G method. For the W95A and BT models, the step size was set to 2.5, while for the W95B model, a logarithmic spacing was applied over 150 steps. Figure 7 shows the largest inner radius of the ROA for the three models.

The proposed GKE-G method is compared with other stability calculation methods. For the W95A and BT models, it yields nearly identical allowable perturbation levels as the SOS1 method employed by Kalur *et al.* (2021), indicating that these are the largest provable ROA utilising quadratic Lyapunov functions.

Kalur *et al.* (2021) also applied the QC method to the same W95A and BT models, predicting significantly smaller regions due to the approximation of nonlinear terms using bounds, despite its lower computational cost. A comparative analysis of the QC method across different model dimensions (TTRD', W95A, BT) reveals a decreasing accuracy with increasing model complexity.

For the W95B model, the calculated allowable perturbation levels are compared with the results of Nerli *et al.* (2007). The presented GKE-G implementation slightly outperforms the GKE method of Nerli *et al.* (2007) due to a more general energy function form. (It is mentioned that Nerli *et al.* (2007) defined the kinetic energy with a multiplier of  $1/2$  which was compensated by a factor of  $1/\sqrt{2}$  on the plots here.) Additionally, the calculated allowable threshold energy levels by the GKE-G method are close to the energy levels of minimal seeds calculated by Cossu (2005). Since the minimal seeds represent states with the lowest kinetic energy converging to another attractor, the close agreement between stability threshold energy and minimal seed energy indicates accurate approximation of the stability region boundary. Similar observations hold for the BT model, where minimal seeds (MS) are calculated by Kalur *et al.* (2021) using direct-adjoint looping.

In contrast, the results for the W95A model show different behaviour. Solutions initialised outside the predicted ROA tend to a laminar state, as also observed by Kalur *et al.* (2021). This suggests that the true ROA is significantly larger than the predicted and might be better captured using higher-order Lyapunov functions.

In summary, the GKE-G method accurately predicts perturbation thresholds for the two-dimensional TTRD' model and the four-dimensional BT and W95B models. However, for the W95A model, the method proves overly conservative, necessitating higher-order Lyapunov functions to capture a larger ROA.

### 3.2. Poiseuille flow models

To construct a reasonably accurate yet comparatively low-dimensional model of the two-dimensional Poiseuille flow we will use Galerkin projection on the basis of eigenfunctions of the Stokes operator. The construction method is described in Appendix B.

The chosen dimension of the domain is  $L_x = 2\pi$  to ensure that the base wavenumber ( $\alpha_0 = 2\pi/L_x = 1$ ) aligns closely with the critical value identified through linear stability analysis, which is  $\alpha = 1.02$  according to Orszag (1971).

To determine an appropriate number of modes for the analysis, an initial assessment was conducted on the reduced-order model's linear stability, followed by an examination of the original energy stability.

Initially, the linear stability limit ( $Re_L$ ) is determined by identifying when the first eigenvalue of the linear part (**A**) turns positive. The influence of the number of modes at a particular wavenumber pairs,  $N_y$  within the range of 10–50 is depicted in table 1. It becomes apparent that, for fewer than 30 modes, the outcome of the linear stability analysis is markedly sensitive to the mode count, a phenomenon attributable to the high susceptibility of the non-normal linear operator to numerical inaccuracies, as highlighted by Trefethen & Embree (2005).

Concurrently, the energy stability limit ( $Re_E$ ) exhibits less sensitivity to the choice of modes  $N_y$  and numerical errors. Notably, as the number of streamwise modes  $N_x$  is increased from 1 to 2, a significant shift in the limit from 121 to 87 is observed. However,

$N_x$	$N_y$	$N$	$Re_L$	$Re_E$
1	10	30	4544.82	121.617
1	20	60	3452.81	121.124
<b>1</b>	<b>30</b>	<b>90</b>	<b>5770.67</b>	<b>121.072</b>
1	40	120	5973.48	121.059
1	50	150	5926.84	121.054
<b>2</b>	<b>30</b>	<b>150</b>	<b>5770.67</b>	<b>87.7574</b>
<b>3</b>	<b>30</b>	<b>210</b>	<b>5770.67</b>	<b>87.7574</b>
<b>4</b>	<b>30</b>	<b>270</b>	<b>5770.67</b>	<b>87.7574</b>
<b>5</b>	<b>30</b>	<b>330</b>	<b>5770.67</b>	<b>87.7574</b>
<b>6</b>	<b>30</b>	<b>390</b>	<b>5770.67</b>	<b>87.7574</b>
<b>7</b>	<b>30</b>	<b>450</b>	<b>5770.67</b>	<b>87.7574</b>
<b>8</b>	<b>30</b>	<b>510</b>	<b>5770.67</b>	<b>87.7574</b>
<b>16</b>	<b>30</b>	<b>990</b>	<b>5770.67</b>	<b>87.7574</b>

Table 1. The critical Reynolds numbers, as determined through linear stability analysis ( $Re_L$ ) and energy stability analysis ( $Re_E$ ), for the two-dimensional PFM with domain size  $L_x = 2\pi$  and  $N_z = 0$ . Values selected for further analysis in this study are highlighted in bold.

further increments in the number of streamwise modes do not influence the outcome. This indicates that the critical perturbation for classical energy analysis corresponds to a wavenumber of  $2\alpha_0 = 2$ , whereas, according to linear stability analysis, the streamwise wavenumber of the critical perturbation is  $\alpha_0 = 1$  for this configuration.

These two limits serve as pivotal benchmarks for the model and can be calculated with relative ease. Below the energy stability limit, the flow is deemed unconditionally stable, implying an infinite radius for the ROA. Conversely, beyond the linear stability limit, the flow becomes unconditionally unstable, reducing the radius of the ROA to zero. Within the bounds of these two limits, the proposed method offers a viable approach to ascertain the conditional stability threshold.

For the models under consideration, the threshold amplitudes are computed with  $N_y = 30$ . This provides a balance between the error margin of the linear stability limit and the number of modes.

The evaluation of the models spans Reynolds numbers from 250 to 2000, in increments of 250. Given the complexity associated with a high number of degrees of freedom, which reaches 90 for the smallest model studied, the SOS methods are deemed impractical for estimating the threshold amplitude. Instead, the GKE-G method is utilised for models up to  $N_x = 5$ , where the results indicate convergence. For demonstration purposes, the GKE-SV method is applied to the largest systems up to  $N_x = 16$  and  $n = 990$ .

The figure 8(a) presents the allowable perturbation amplitude for various models at  $Re = 500$ . It depicts the square root of the ratio of allowable perturbation kinetic energy to the base flow kinetic energy ( $E$ ), essentially showcasing the proportionality between the magnitude of perturbation velocity and the base flow velocity. This metric is henceforth referred to as the threshold amplitude ratio.

In the application of the GKE-G method, notable variations in results persist until the number of degrees of freedom reaches 210 ( $N_x = 3$ ), beyond which increases to 270 ( $N_x = 4$ ) or 330 ( $N_x = 5$ ) result in only slight changes. It is important to note that the optimisation process of the transformation matrix does not utilise results from lower-order dynamical systems, rendering these results independently obtained. The convergence of the threshold amplitude ratio, therefore, suggests that the optimisation either identifies

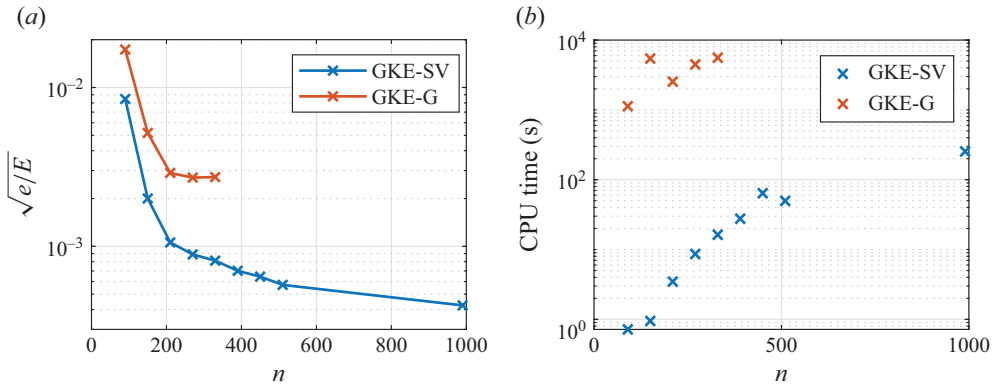


Figure 8. (a) The square root of the ratio of allowable perturbation kinetic energy to the base flow kinetic energy, plotted as a function of degrees of freedom for a two-dimensional Poiseuille flow at  $Re = 500$ . The periodic domain length is set to  $L_x = 2\pi$ . (b) The computational time required for the analysis.

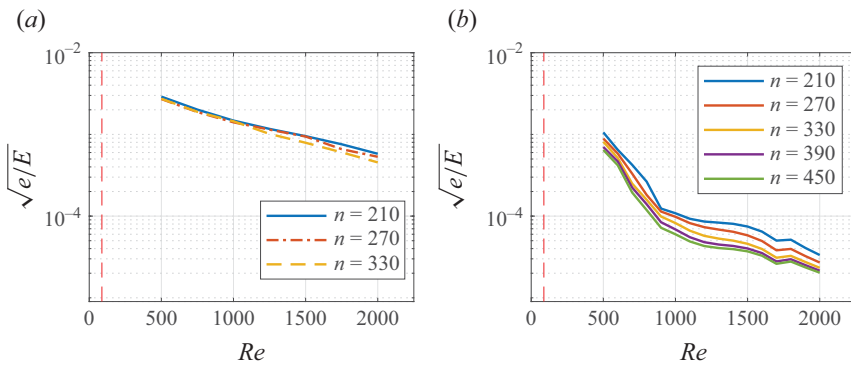


Figure 9. The square root of the ratio of allowable perturbation kinetic energy to the base flow kinetic energy plotted against the Reynolds number for various PFMs. The transformation matrix optimisation is carried out using (a) the GKE-G method and (b) the GKE-SV method.

the global maximum of the allowable perturbation level or converges to a similar local maximum across various system sizes.

When the transformation matrix is optimised using the GKE-SV method, the predicted allowable perturbation level is lower, as anticipated. This reduction is due to the optimisation focusing solely on the singular values of the  $\Psi$  matrix and considering only the linear component of the dynamical system. However, these substantial simplifications in determining the optimal transformation matrix yield a threshold amplitude that is less than one magnitude smaller than that predicted by the GKE-G method. Conversely, the previously described QC method predicts significantly lower threshold amplitude levels, even for smaller dynamical systems.

Figure 8(b) compares the computational times between the two optimisation approaches. The benefits of employing the GKE-SV method are evident; not only is the computational time orders of magnitude lower, but it also facilitates application to larger dynamical systems, underscoring its efficiency and scalability.

Next, the threshold amplitude ratio as a function of Reynolds number is depicted in figure 9. When the transformation matrix is optimised using the GKE-G method for models with  $n = 210, 270, 330$ , the resulting curves closely align with one another, with

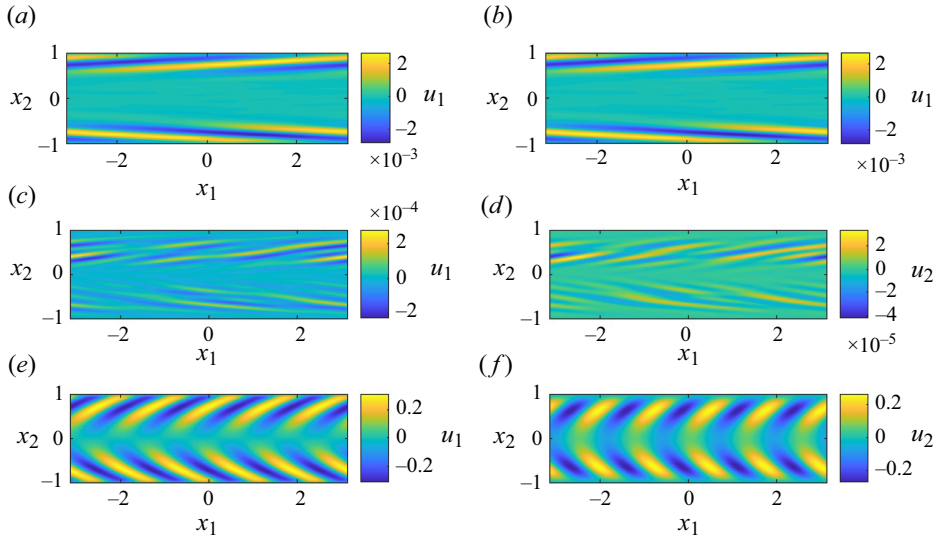


Figure 10. Perturbation field for the truncated PFM with  $n = 330$  at  $Re = 1000$ . Panels (a) and (b) show the states with the smallest energy ( $e_{min}$ ) on the boundary of provable ROA calculated using the GKE-G method. Panels (c) and (d) depict the same states using the GKE-SV method. Panels (e) and (f) present the perturbations with the highest growth rate according to the original energy method. The streamwise and wall-normal velocity components are shown in the left and right columns, respectively.

only minor deviations observed at higher Reynolds numbers. The figure plots the threshold amplitude ratio on a logarithmic y-axis against a linear x-axis. The nearly linear curves suggest a decay rate faster than a power law, consistent with the flow's linear instability at a finite Reynolds number, where the threshold amplitude approaches zero.

In figure 9(a), the threshold amplitudes obtained using the GKE-SV method are presented. The amplitude ratios are notably lower than those calculated via the GKE-G method, which can be attributed to the simpler optimisation process previously discussed. Additionally, fluctuations are observed around at  $Re = 1700$ , highlighting the sub-optimality of the GKE-SV method. These fluctuations result from the restrictions imposed on the transformation matrix, which vary with the Reynolds number but remain consistent across the models since they describe the same shear flow configuration. As the Reynolds number increases, the disparity between the results from the two methods widens, yet the difference remains under two magnitudes even at the highest Reynolds number evaluated.

The findings are juxtaposed with the minimal seed calculations conducted by Zhang & Tao (2023), who determined that the laminar flow remains globally stable up to a Reynolds number of 2332.5. Zhang calculated the energy of the minimal seed at  $Re = 2333$  to be approximately  $e_{MS} = 0.01$ . From this value, the estimated amplitude ratio of the minimal seed,  $\sqrt{e_{MS}/E}$ , is roughly 0.007. This represents the amplitude limit beyond which perturbations persist within the system. In our analysis utilising the 330-dimensional model with the GKE-G method, the threshold amplitude – up to which the laminar flow maintains stability – is approximately  $\sqrt{e_{min}/E} = 0.00045$  at  $Re = 2000$ . This value is only one magnitude smaller than the minimal seed estimation. However, it is important to note that their results were obtained in a significantly larger domain of  $L_x = 400$ , compared with the domain length of  $L_x = 2\pi$  employed in our study.

In figure 10, panels (a–d) present the perturbations with the smallest kinetic energy ( $e_{min}$ ) at the boundary of the provable ROA for both the GKE-G and GKE-SV methods.

Source	Perturbation	Domain	$Re$ range	$\eta$
Lundbladh <i>et al.</i> (1994)	Oblique wave	$2\pi \times 2 \times 2\pi$	1500–5000	−1.75
Reddy <i>et al.</i> (1998)	Oblique wave	$2\pi \times 2 \times 2\pi$	1500–5000	−1.6
Parente <i>et al.</i> (2022)	Minimal seed	$250 \times 2 \times 125$	1000–1568	−4.25
Zhang & Tao (2023)	Minimal seed	$100 \times 2$ (2D)	2500–4500	−3.8
PFM $n = 330$	GKE-G stability	$2\pi \times 2$ (2D)	500–2000	−1.28

Table 2. Exponents of the power law for the threshold amplitude ( $\sqrt{e_{min}} \propto Re^{-\eta}$ ), corresponding to half of the exponents for the threshold energy.

In the case of the GKE-G method, these perturbations manifest as tilted periodic waves localised near the walls, resembling the minimal seed states described by Zhang & Tao (2023). However, due to the significantly longer domain (100 units) used in their study, sometimes localised structures in the streamwise direction were observed, depending on the initial perturbation amplitude and Reynolds number. The shorter domain length ( $2\pi$ ) in our study likely excludes the observation of such structures, resulting in fully periodic structures instead.

For the GKE-SV method, the perturbations appear as stripes localised between the wall and the domain's centreline. These perturbations are less structured and exhibit asymmetry, likely due to the sub-optimal nature of the GKE-SV method.

For reference, panels (e–f) in figure 10, show the critical perturbation with the highest growth rate ( $\mu_e = 0.7712$ ) according to the original energy method. These perturbations also appear as tilted periodic waves, as demonstrated by Farrell (1988), but are less localised to the near-wall region and exhibit higher oscillations in the streamwise direction compared with the critical perturbations according to the GKE-G method.

In the following phase of the analysis, power-law functions are fitted to the threshold amplitude as a function of Reynolds number,  $\sqrt{e} \propto Re^\eta$ . This fitting method has previously shown effectiveness for Couette flow, as documented by Duguet *et al.* (2013), and has been employed in other referenced studies. For Poiseuille flow, the exponents derived from the fitting range between −1.6 and −4.25, according to research conducted by Lundbladh *et al.* (1994), Reddy *et al.* (1998), Parente *et al.* (2022) and Zhang & Tao (2023).

The exponents predicted using the GKE-G method surpass these cited figures, yielding an exponent of −1.28 for the model with  $n = 330$  dimensions. This discrepancy could stem from several factors. Notably, the current investigation focuses on two-dimensional flow, and the range of Reynolds numbers considered also differs. Additionally, as previously discussed, the relationship between threshold amplitude and Reynolds number in Poiseuille flow is likely to diverge from a simplistic power-law function, further contributing to the observed differences.

#### 4. Conclusion

Due to the subcritical nature of the most shear flows, the calculation of the allowable perturbation level is an important scientific challenge. Minimal seed calculations by nonlinear optimisation have proven to be an efficient tool for that; however, the validation of the result still needs alternative methods. This study introduces an approach for determining the conditional stability limit of laminar flows by constructing a quadratic Lyapunov function. The method of Nerli *et al.* (2007) is followed to validate the Lyapunov function through nonlinear optimisation; however, in this study, it is defined in a more

general form by applying a linear transformation to the state variables and establishing a generalised kinetic energy via the inner product of the transformed variables.

The transformation directly impacts the growth rate of generalised kinetic energy, making it dependent on the perturbation amplitude. This dependency allows for the calculation of the threshold amplitude of stability, offering vital insights into the system's dynamics. With a suitable definition of the generalised kinetic energy through the transformation matrix, the maximum potential growth rate of infinitesimal perturbations is negative (if  $Re < Re_L$ ) and it increases with the perturbation level. The maximum potential growth rate of the system, relative to the perturbation level, delineates two distinct regions: an initial phase dominated by a linear dynamics at lower perturbation levels, followed by a transitional phase to a regime where nonlinear effects predominate at higher levels. The critical perturbation level, below which the laminar state remains stable, is defined by the intersection of the maximum generalised kinetic energy growth rate with the zero line.

In the transformed state space, the basin of attraction is a hypersphere with a radius equal to the critical perturbation level, whereas, in the original state space, it is a hyperellipsoid with the smallest semiminor axis dictating the maximum allowable perturbation kinetic energy. To optimise this threshold, two strategies are delineated: the GKE-SV method, which optimises the singular values of the linear system's eigenvector matrix, and the GKE-G method, which optimises the elements of a general triangular transformation matrix through the interior-point algorithm, utilising analytic gradients for efficiency.

A crucial part of the calculations involves determining the global maximum of the potential growth rate across a variety of perturbation states. To ensure precision, this methodology integrates the use of analytic gradients and the Hessian matrix, alongside employing multiple seed locations for a thorough exploration of the solution space. In this context, three renowned optimisation algorithms were evaluated, with the SQP method and the interior-point algorithm recommended for small and large dynamical systems, respectively.

When juxtaposed with traditional SOS programs, it emerges that the presented GKE methods give no significant benefits for smaller systems. However, they prove to be viable for larger systems, where  $n > 20$ , a domain where SOS methods typically falter.

The GKE-G method was applied to the well-known low-dimensional systems: the TTRD' model and three different variations of the four-dimensional Waleffe model. In general, the proposed method predicts a similar allowable threshold amplitude as the SOS methods and significantly larger than so-called QC method. Additionally, for the TTRD' model and the W95B and BT parameter sets of the Waleffe model, the proximity of the minimal seed solutions to the boundary of the calculated ROA reinforces the accuracy of the GKE-G methodology.

Applying GKE methods to a reduced-order model of two-dimensional Poiseuille flow (90–990 degrees of freedom) shows that the GKE-G method accurately calculates the perturbation threshold with 330 modes. Moreover, the calculated critical perturbation shape qualitatively aligns with minimal seed solutions from the literature.

The GKE-SV method predicts a much lower threshold amplitude at a fraction of the computational cost, with the divergence increasing at higher Reynolds numbers but staying within two orders of magnitude, even for the largest systems analysed.

In summary, the presented methodology for constructing quadratic Lyapunov functions can be applied to significantly larger fluid dynamical systems than SOS techniques. Nonetheless, challenges persist in three-dimensional domains due to the reliance on high-dimensional models. Employing more efficient basis functions, like controllability modes (Cavaleri & Nogueira 2022) instead of Stokes modes, could reduce the necessary

model order, potentially enabling the analysis of finite-dimensional models for three-dimensional flows with the presented GKE methods. Future improvements might involve the use of infinite-dimensional models (Goulart & Chernyshenko 2012; Fuentes *et al.* 2022), considering the worst-case effects of truncated modes on flow stability. Notably, Fuentes *et al.* (2022) demonstrated a significantly higher global stability limit for two-dimensional Couette flow using only 13 modes. Given that the GKE method can efficiently handle systems with several hundred modes, extending it to accommodate infinite-dimensional models could potentially uncover the conditional stability of physically relevant three-dimensional flows.

**Acknowledgements.** The author is grateful to Y. Duguet at CNRS and David Goluskin at University of Victoria for their helpful recommendations. Furthermore, the author would like to express their sincere gratitude to the anonymous reviewers for their insightful comments, constructive suggestions and valuable time dedicated to reviewing this manuscript. Their feedback has significantly contributed to improving the clarity and quality of this work.

**Funding.** This paper was supported by the János Bolyai Research Scholarship of the Hungarian Academy of Sciences. The research leading to these results received funding from the National Research Development and Innovation Office of Hungary under Grant Agreement no. K142675.

**Declaration of interests.** The author reports no conflict of interest.

## Appendix A. Numerical methods

### A.1. The maximisation of $\mu_h$

The critical aspect of the method lies in determining the maximum potential growth rate of GKE (2.24). In practical implementations, Matlab's *fmincon* is employed, a tool that can significantly benefit from the provision of gradient and Hessian matrix of the cost function. The derivatives of the growth rate (2.23) concerning the normalised state vector ( $\tilde{r}_k$ ) are expressed as follows:

$$\frac{\partial \mu_h}{\partial \tilde{r}_p} = 2(\tilde{A}_{p,i} + \tilde{A}_{i,p})\tilde{r}_i + 2\gamma(S_{ij}^{-1}Q_{jkl}S_{kp}S_{lo}\tilde{r}_o\tilde{r}_i + S_{ij}^{-1}Q_{jkl}S_{km}\tilde{r}_mS_{lp}\tilde{r}_i + S_{pj}^{-1}Q_{jkl}S_{km}\tilde{r}_mS_{lo}\tilde{r}_o), \quad (A1)$$

where  $\tilde{A}_{ij}$  is the transformed  $A_{ij}$  matrix defined in equation (2.19). Let us introduce the vectors  $v_j = S_{ji}^{-T}\tilde{r}_i$  and  $\tilde{q}_i = S_{ij}\tilde{r}_j$  to simplify the gradient

$$\frac{\partial \mu_h}{\partial \tilde{r}_p} = 2(\tilde{A}_{pi} + \tilde{A}_{ip})\tilde{r}_i + 2\gamma(S_{pk}^TQ_{jkl}\tilde{q}_l v_j + S_{pl}^TQ_{jkl}\tilde{q}_k v_j + S_{pj}^{-1}Q_{jkl}\tilde{q}_k\tilde{q}_l). \quad (A2)$$

The Hessian matrix of  $\mu_h$  (2.23) is given by

$$\begin{aligned} \frac{\partial^2 \mu_h}{\partial \tilde{r}_p \partial \tilde{r}_q} = & 2(\tilde{A}_{pq} + \tilde{A}_{qp}) + 2\gamma(S_{ij}^{-1}Q_{jkl}S_{kp}S_{lq}\tilde{r}_i + S_{qj}^{-1}Q_{jkl}S_{kp}S_{lo}\tilde{r}_o \\ & + S_{ij}^{-1}Q_{jkl}S_{kq}S_{lp}\tilde{r}_i + S_{qj}^{-1}Q_{jkl}S_{km}\tilde{r}_mS_{lp} + S_{pj}^{-1}Q_{jkl}S_{kq}S_{lo}\tilde{r}_o \\ & + S_{pj}^{-1}Q_{jkl}S_{km}\tilde{r}_mS_{lq}). \end{aligned} \quad (A3)$$

By introducing the expressions

$$B_{kl} = Q_{jkl}v_j, \quad C_{jk} = Q_{jkl}\tilde{q}_l, \quad D_{jl} = Q_{jkl}\tilde{q}_k, \quad (A4)$$

the equation (A3) simplifies to

$$\begin{aligned} \frac{\partial^2 \mu_h}{\partial \tilde{r}_p \partial \tilde{r}_q} = & 2(\tilde{A}_{pq} + \tilde{A}_{qp}) + 2\gamma (S_{pk}^T B_{kl} S_{lq} + (S_{qj}^{-1} C_{jk} S_{kp})^T \\ & + (S_{qk}^T B_{kl} S_{lp})^T + (S_{pj}^{-1} D_{jl} S_{lp})^T + S_{pj}^{-1} C_{jk} S_{kq} + S_{pj}^{-1} D_{jl} S_{lq}). \end{aligned} \quad (\text{A5})$$

It is worth noticing that the Hessian matrix consists of the sum of four matrices and their transposes, resulting in a symmetric expression. This symmetry is expected due to the nature of second derivatives. From a practical perspective, only half of the expression needs to be calculated; the other half can be obtained by transposing the appropriate matrices.

The optimisation is constrained by the requirement that the transformed state vector should be unitary

$$c = \tilde{r}_i \tilde{r}_i - 1 = 0. \quad (\text{A6})$$

The gradient of the constraint is straightforward

$$\frac{\partial c}{\partial \tilde{r}_i} = 2\tilde{r}_i. \quad (\text{A7})$$

The Hessian of the constraint (A6) is given by

$$\frac{\partial^2 c}{\partial \tilde{r}_i \partial \tilde{r}_j} = 2\delta_{i,j}, \quad (\text{A8})$$

where  $\delta_{i,j}$  is the Kronecker delta function and the right-hand side is two times the identity matrix.

#### A.2. The maximisation of $e_{min}$

The maximisation of  $e_{min}(S_{ij})$  (2.30) through the GKE-G method is substantially enhanced by employing gradient-based optimisation. The sensitivity of  $e_{min}$  to variations in the transformation matrix is derived from equation (2.30) as

$$\frac{\partial e_{min}}{\partial S_{ij}} = 2\gamma_{crit} \frac{\partial \gamma}{\partial S_{ij}} \lambda_{min} + \gamma_{crit}^2 \frac{\partial \lambda_{min}}{\partial S_{ij}}. \quad (\text{A9})$$

The sensitivity of the  $\lambda$  can be expressed as

$$\frac{\partial \lambda}{\partial S_{ij}} = 2S_{ik} r_{min,j} r_{min,k}, \quad (\text{A10})$$

where  $r_{min}$  is the eigenvector associated with the smallest eigenvalue of  $\mathbf{S}^T \mathbf{S}$ . The gradient of  $\gamma$  with respect to the transformation matrix is determined as

$$\frac{\partial \gamma}{\partial S_{ij}} = -\frac{\partial \mu_{h,max}}{\partial S_{ij}} \frac{1}{\frac{\partial \mu}{\partial \gamma}}. \quad (\text{A11})$$

The derivatives of the growth rate (2.26) with respect to the elements of the transformation matrix are calculated as follows:

$$\begin{aligned} \frac{\partial \mu_{h,max}}{\partial S_{pq}} = & 2(-\tilde{r}_i S_{ip}^{-1} S_{qj}^{-1} A_{jm} S_{mo} \tilde{r}_o + \tilde{r}_i S_{ij}^{-1} A_{jp} \tilde{r}_q) \\ & + 2\gamma(-\tilde{r}_i S_{ip}^{-1} S_{ql}^{-1} Q_{lmo} S_{mp} \tilde{r}_p S_{or} \tilde{r}_r + \tilde{r}_i S_{ij}^{-1} Q_{jpl} \tilde{r}_q S_{lo} \tilde{r}_o \\ & + \tilde{r}_i S_{ij}^{-1} Q_{jkm} S_{km} \tilde{r}_m \tilde{r}_q), \end{aligned} \quad (A12)$$

where it was assumed the inverse of a slightly perturbed transformation matrix can be approximated as

$$(S_{ij} + \delta S_{ij})^{-1} \approx S_{ij}^{-1} - S_{ik}^{-1} \delta S_{kl} S_{lj}^{-1}. \quad (A13)$$

Simplifying these expressions (A12) using predefined vectors and the transformed  $A_{ij}$  results in

$$\begin{aligned} \frac{\partial \mu_{h,max}}{\partial S_{pq}} = & 2(-v_p \tilde{A}_{qj} \tilde{r}_j + v_j A_{jp} \tilde{r}_q) \\ & + 2\gamma(-v_p S_{ql}^{-1} Q_{lmo} \tilde{q}_m \tilde{q}_o + v_j Q_{jpl} \tilde{r}_q \tilde{q}_l + v_j Q_{jkm} \tilde{q}_k \tilde{r}_q). \end{aligned} \quad (A14)$$

Moreover, the derivative of the growth rate with respect to the perturbation level is

$$\frac{\partial \mu_{h,max}}{\partial \gamma} = 2\gamma \tilde{Q}_{ijk} \tilde{r}_i \tilde{r}_j \tilde{r}_k, \quad (A15)$$

which is simply the nonlinear component of  $\mu_h$

$$\frac{\partial \mu_{h,max}}{\partial \gamma} = \mu_{h,NL}. \quad (A16)$$

The derivatives presented in equations (A14) and (A15) are evaluated at the critical perturbation that maximises the growth rate,  $\mu_h$ .

### A.2.1. First sum-of-squares program

The first (SOS) program, widely used to calculate the ROA for conditionally stable systems (Jarvis-Wloszek 2003; Tan & Packard 2008; Topcu *et al.* 2008; Khodadadi *et al.* 2014; Kalur *et al.* 2021), is delineated as follows:

$$V - l_1 \in \Sigma, \quad (A17)$$

$$-[(\beta - p)s_1 + (V - \gamma^2)] \in \Sigma, \quad (A18)$$

$$-((\gamma^2 - V)s_2 + \dot{V}s_3 + l_2) \in \Sigma. \quad (A19)$$

The following three paragraphs provide a brief description of the method, along with the new expressions and notations. Here,  $V$  represents the conditional Lyapunov function, akin to  $h$  in the GKE method but potentially non-quadratic, contrasting with the strictly quadratic nature of  $h$  in the GKE method. The derivative of  $V$  with respect to time is denoted as  $\dot{V}$

$$\dot{V} = \frac{\partial V}{\partial q_i} \frac{dq_i}{dt}. \quad (A20)$$

The polynomials  $l_1$  and  $l_2$  are predefined positive definite to ensure positive definiteness (rather than semi-definiteness) of the expressions, set to  $l_i = 10^{-10} \mathbf{q}^T \mathbf{q}$  for minimal impact on results. The variable  $\beta$  indicates the ROA's size, with  $p$  depicting its shape, typically chosen as  $p = \mathbf{q}^T \mathbf{q}$  to describe a supersphere, thus approximating the ROA similar to the generalised kinetic energy methods with  $\beta = e_{min}$ . The parameter  $\gamma$  specifies the

state space region where the Lyapunov function decreases along the system's solution trajectories.

Equation (A17) asserts that the Lyapunov function  $V$  must be positive definite. Equation (A18) is employed to maximise  $\beta$  for the largest possible ROA shaped by the polynomial  $p$ . Equation (A19) mandates that the Lyapunov function decreases along the solution trajectories within the region where  $V < \gamma^2$ . The symbols  $s_1, s_2, s_3$  represent positive semi-definite polynomials.

The notation ' $\in \Sigma$ ' signifies that the left-hand side must be expressible in a SOS form, thereby being positive semi-definite. A SOS decomposition enables a polynomial up to degree  $2d$  to be represented as  $\mathbf{m}^T(\mathbf{q}) \mathbf{M} \mathbf{m}(\mathbf{q})$ , with  $\mathbf{m}(\mathbf{q})$  encompassing all monomials up to order  $d$  and  $\mathbf{M}$  a positive definite matrix, leading to matrix inequality constraints during optimisation. While the problem could be reformulated into a SDP solvable efficiently if all constraints were linear, equations (A18–A19) include bilinear terms in polynomial decision variables, necessitating a decomposed optimisation approach over multiple iterations. Initially, the process starts with the  $\gamma$  step, during which  $\gamma$  is treated as a parameter rather than as part of the decision variables. This parameter is maximised using a bisection algorithm until equation (A19) is feasible, indicating that the left-hand side can be represented as a SOS expression. Following this, the  $\beta$  step commences, setting  $\beta$  as a parameter and employing a bisection algorithm to maximise it until equation (A18) is satisfied, using the maximal  $\gamma$  value determined in the previous step. The final phase is the  $V$  step, where all equations from (A17) to (A19) are addressed. However, in this phase, decision variables established in earlier steps are held constant, with the exception of the Lyapunov function  $V$ , which undergoes updates. This sequence of steps is iterated until  $\beta$  reaches its peak, and the relative change dips below the set tolerance level of  $10^{-3}$ . This iterative algorithm is designated as SOS1 in this study.

### A.2.2. Second sum-of-squares program

In the context of quadratic Lyapunov functions, an alternative approach has been proposed by Liu & Gayme (2020). This approach adopts the same definition of the Lyapunov function as in the GKE method, with  $V = h$ , as outlined in equation (2.14). The corresponding SOS program is presented as follows:

$$V - l_1 \in \Sigma, \quad (\text{A21})$$

$$-(\dot{V} + (\delta^2 - \mathbf{q}^T \mathbf{q})s_1 + l_2) \in \Sigma. \quad (\text{A22})$$

The first equation (A21) ensures the positive definiteness of the Lyapunov function ( $V$ ), analogous to equation (A17). The subsequent equation, (A22), mandates that  $\dot{V}$  is negative within a specific region, the size of which is proportional to  $\delta^2$ . However, this region is not the ROA since, although  $\dot{V} < 0$ ,  $d/dt(\|\mathbf{q}\|)$  can be positive in this region and trajectories can go outwards. The provable ROA is a subset of this region where  $V < \gamma^2$ . Here,  $\gamma$  can be calculated from the definition of  $V$  as  $\gamma^2 = \lambda_{\min}(P) \delta^2$ . This approach replaces and simplifies the second equation (A18) of SOS1 leading to faster but less accurate results.

The calculated ROA forms a superellipsoid analogous to that in the GKE method. The radius of the largest supersphere contained within this superellipsoid is given by  $\sqrt{e_{\min}} = \delta \sqrt{\lambda_{\min}(P)/\lambda_{\max}(P)}$ .

Like SOS1, (A22) introduces a nonlinear constraint on the decision variables due to the inclusion of the term  $\delta^2 s_1$ . To address this,  $\delta^2$  is considered as a parameter rather than a decision variable and is maximised using a bisection algorithm until (A22) is feasible. This SOS program is referred to as SOS2 in the study.

## Appendix B. Construction of Poiseuille flow model

The Stokes equations in non-dimensional form are given by

$$\frac{\partial u_i}{\partial t} = -\frac{\partial p}{\partial x_i} + \frac{1}{Re} \frac{\partial^2 u_i}{\partial x_j \partial x_j}, \quad (\text{B1})$$

and

$$\frac{\partial u_i}{\partial x_i} = 0, \quad (\text{B2})$$

where  $u_i$  represents the non-dimensional velocity,  $p$  is the non-dimensional pressure and  $x_i$  are the spatial coordinates:  $x_1 \in [0, L_x]$ ;  $x_2 \in [-1, 1]$ ;  $x_3 \in [0, L_z]$ , defining a rectangular cuboid. The eigenvectors can be obtained by assuming the following ansatz:

$$u_i = \hat{u}_i e^{\lambda t}, \quad (\text{B3})$$

and solving the eigenvalue problem

$$\lambda \hat{u}_i = -\frac{\partial \hat{p}}{\partial x_i} + \frac{1}{Re} \frac{\partial^2 \hat{u}_i}{\partial x_j \partial x_j}, \quad (\text{B4})$$

$$\frac{\partial \hat{u}_i}{\partial x_i} = 0, \quad (\text{B5})$$

for  $\lambda$ . The eigenvalues are negative real numbers expressing the dissipation rate of the mode. Furthermore, the eigenvectors are orthogonal, which proves advantageous for Galerkin projection. Given the linearity of the eigenvalue problem and assuming periodic solutions in the  $x_1$  and  $x_3$  directions, solving the eigenvalue problem is conveniently achieved using complex Fourier series. The modes of the  $\hat{u}_i$  velocity field can be expressed as follows:

$$\tilde{u}_{i j_m k_m}(x_2) e^{i(j_m \alpha_0 x_1 + k_m \beta_0 x_3)}, \quad (\text{B6})$$

where  $\alpha_0 = 2\pi/L_x$  and  $\beta_0 = 2\pi/L_z$  are the wavenumbers, and  $j_m, k_m$  are the indices of the modes ranging from  $-\infty$  to  $\infty$ . Substituting the complex wave form (B6) into equations (B2) and (B4) leads to the following eigenvalue problem for each  $j_m, k_m$  mode

$$\begin{bmatrix} L & 0 & 0 & -i\alpha \\ 0 & L & 0 & -D_{x_2} \\ 0 & 0 & L & -i\beta \\ i\alpha & D_{x_2} & i\beta & 0 \end{bmatrix} \begin{bmatrix} \tilde{u}_1 \\ \tilde{u}_2 \\ \tilde{u}_3 \\ \tilde{p} \end{bmatrix} = \lambda \begin{bmatrix} 1 & 0 & 0 & 0 \\ 0 & 1 & 0 & 0 \\ 0 & 0 & 1 & 0 \\ 0 & 0 & 0 & 0 \end{bmatrix} \begin{bmatrix} \tilde{u}_1 \\ \tilde{u}_2 \\ \tilde{u}_3 \\ \tilde{p} \end{bmatrix}, \quad (\text{B7})$$

where  $\alpha = j_m \alpha_0$ ,  $\beta = k_m \beta_0$  and  $L = -(\alpha^2 + \beta^2) + D_{x_2}^2$  is the Laplace operator, where  $D_{x_2}$  is the differential operator with respect to  $x_2$ .

The problem (B7) can be discretised using the Chebyshev collocation method. The required boundary conditions involve stationary walls at the bottom and top of the domain, implying  $\tilde{u}_i(\pm 1) = 0$  for any  $i$  velocity component. These conditions are enforced by removing the corresponding rows from the matrices. In this study, 100 Chebyshev collocation points are employed, a choice deemed accurate based on prior research (Nagy & Kulcsár 2023). The discretised version of the equations (B7) solved for the first  $N_y$  modes with the largest  $\lambda$  eigenvalues for  $j_m \in [-N_x, N_x]$  and  $k_m \in [-N_z, N_z]$  resulting in a total of  $n = (2N_x + 1) N_y (2N_z + 1)$  modes. The calculation can be simplified, since in the case of complex-conjugate wavenumber pairs ( $j_{m,a} = -j_{m,b}$  and  $k_{m,a} = -k_{m,b}$ ), the eigenvalues are the same and the eigenvectors are the complex conjugate of each other  $\tilde{u}_{i j_m k_m} = \tilde{u}_{i -j_m -k_m}^*$ . The values of the parameters ( $N_x, N_y, N_z$ ) vary across different

models and will be provided later. Subsequently, the coefficients  $A_{ij}$  and  $Q_{ijk}$  are computed using the Galerkin projection method

$$A_{i_m j_m} = \int_{\Omega} \left( -U_j \frac{\partial \hat{u}_{i_m}}{\partial x_j} - \hat{u}_{j_m} \frac{\partial U_i}{\partial x_j} + \frac{1}{Re} \frac{\partial^2 u_{i_m}}{\partial x_j \partial x_j} \right) \hat{u}_{i_m}^* d\Omega, \quad (B8)$$

$$Q_{i_m j_m k_m} = \int_{\Omega} \left( -\hat{u}_{j_m} \frac{\partial \hat{u}_{i_m}}{\partial x_j} \right) \hat{u}_{k_m}^* d\Omega, \quad (B9)$$

where  $i_m$ ,  $j_m$  and  $k_m$  are the indices of the modes,  $U_i$  denotes the velocity field of the base flow and  $\hat{u}_{i_m}^*$  is the complex conjugate of  $\hat{u}_{i_m}$ . For the Poiseuille flow investigated in this study, having only one non-zero velocity component

$$U_1 = 1 - x_2^2. \quad (B10)$$

It is worth noting that

$$\int_{\Omega} \frac{\partial^2 u_{i_m}}{\partial x_j \partial x_j} \hat{u}_{i_m}^* d\Omega = \lambda_{i_m} \delta_{i_m, j_m}. \quad (B11)$$

This is due to the fact that the velocity modes are eigensolutions of the Stokes operator, equations (B4) and (B5).

The modes are substituted in the form (B6) and the integrals over  $x_2$  are evaluated utilising Chebyshev collocation points. Since the eigenvectors are complex, the  $A_{ij}$  matrix and the  $Q_{ijk}$  tensor are also complex. As a result, the previously derived gradients for the optimisation procedure become invalid. However, this issue can be resolved by transforming the system into a real-valued one. Let  $i_0$  represent the indices of the real-valued modes,  $i_c$  the complex-valued modes and  $i_{cc}$  their corresponding complex conjugates. By rearranging the modes in the order  $i_0, i_c, i_{cc}$ , a transformation matrix  $\mathbf{T}$  can be defined as follows:

$$\mathbf{T} = \begin{bmatrix} T_{i_0 i_0} & T_{i_0 i_c} & T_{i_0 i_{cc}} \\ T_{i_c i_0} & T_{i_c i_c} & T_{i_c i_{cc}} \\ T_{i_{cc} i_0} & T_{i_{cc} i_c} & T_{i_{cc} i_{cc}} \end{bmatrix} = \begin{bmatrix} \mathbf{I}_{N_0 \times N_0} & \mathbf{0}_{N_0 \times N_c} & \mathbf{0}_{N_0 \times N_c} \\ \mathbf{0}_{N_c \times N_0} & \frac{1}{\sqrt{2}} \mathbf{I}_{N_c \times N_c} & \frac{1}{\sqrt{2}} \mathbf{I}_{N_c \times N_c} \\ \mathbf{0}_{N_c \times N_0} & \frac{1}{i\sqrt{2}} \mathbf{I}_{N_c \times N_c} & -\frac{1}{i\sqrt{2}} \mathbf{I}_{N_c \times N_c} \end{bmatrix}. \quad (B12)$$

Here,  $N_0$  represents the number of real-valued modes, and  $N_c$  represents the number of complex-valued modes (taking into account half of the complex-conjugate pairs). Applying the  $\mathbf{S} = \mathbf{T}^{-1}$  transformation matrix on the problem as described by equations (2.19) and (2.20) results in real-valued  $A_{ij}$  matrix and the  $Q_{ijk}$  tensor, respectively. This transformation matrix can also be used to convert the transformed real coefficients back into the original complex coefficients of the complex-valued modes.

## REFERENCES

- BAGGETT, J.S. & TREFETHEN, L.N. 1997 Low-dimensional models of subcritical transition to turbulence. *Phys. Fluids* **9** (4), 1043–1053.
- CAVALIERI, A.V.G. & NOGUEIRA, P.A.S. 2022 Reduced-order Galerkin models of plane Couette flow. *Phys. Rev. Fluids* **7** (10), L102601.
- CHERUBINI, S., DE PALMA, P. & ROBINET, J.-CH 2015 Nonlinear optimals in the asymptotic suction boundary layer: transition thresholds and symmetry breaking. *Phys. Fluids* **27** (3), 034108.
- COSSU, CARLO 2005 An optimality condition on the minimum energy threshold in subcritical instabilities. *Comptes Rendus Mécanique* **333** (4), 331–336.
- DAUCHOT, O. & MANNEVILLE, P. 1997 Local versus global concepts in hydrodynamic stability theory. *J. Phys. II France* **7** (2), 371–389.

- DRAZIN, P. & REID, W. 2004 *Hydrodynamic Stability*. second edn. Cambridge University Press.
- DUGUET, Y., MONOKROUSOS, A., BRANDT, L. & HENNINGSON, D.S. 2013 Minimal transition thresholds in plane couette flow. *Phys. Fluids* **25** (8), 084103.
- FALSAPERLA, P., GIACOBBE, A. & MULONE, G. 2019 Nonlinear stability results for plane Couette and Poiseuille flows. *Phys. Rev. E* **100** (1), 013113.
- FARRELL, B.F. 1988 Optimal excitation of perturbations in viscous shear flow. *Phys. Fluids* **31** (8), 2093–2102.
- FRATERNALE, F., DOMENICALE, L., STAFFILANI, G. & TORDELLA, D. 2018 Internal waves in sheared flows: lower bound of the vorticity growth and propagation discontinuities in the parameter space. *Phys. Rev. E* **97** (6), 063102.
- SIR W.THOMSON L.L.D., F.R.S. 1887 XXI. stability of fluid motion (continued from the may and june numbers).—rectilinear motion of viscous fluid between two parallel planes. *Lond. Edin. Dublin Phil. Mag. J. Sci.* **24** (147), 188–196.
- FUENTES, F., GOLUSKIN, D. & CHERNYSHENKO, S. 2022 Global stability of fluid flows despite transient growth of energy. *Phys. Rev. Lett.* **128** (20), 204502.
- GALDI, G.P. & PADULA, M. 1990 A new approach to energy theory in the stability of fluid motion. *Arch. Ration. Mech. Anal.* **110** (3), 187–286.
- GALDI, G.P. & STRAUGHAN, B. 1985 Exchange of stabilities, symmetry, and nonlinear stability. *Arch. Ration. Mech. Anal.* **89** (3), 211–228.
- GOULART, P.J. & CHERNYSHENKO, S. 2012 Global stability analysis of fluid flows using sum-of-squares. *Physica D: Nonlinear Phenom.* **241** (6), 692–704.
- HENRION, D. & KORDA, M. 2014 Convex computation of the region of attraction of polynomial control systems. *IEEE Trans. Autom. Control* **59** (2), 297–312.
- HUANG, D., CHERNYSHENKO, S., GOULART, P., LASAGNA, D., TUTTY, O. & FUENTES, F. 2015 Sum-of-squares of polynomials approach to nonlinear stability of fluid flows: An example of application. *Proc. R. Soc. A Math. Phys. Engng Sci.* **471** (2183), 20150622.
- JARVIS-WLOSZEK, Z.W. 2003 Lyapunov based analysis and controller synthesis for polynomial systems using sum-of-squares optimization. PhD thesis, University of California.
- JOSEPH, D.D. 1976 *Stability of Fluid Motions I*. Springer-Verlag, New York.
- JOSEPH, D.D. & CARMI, S. 1969 Stability of Poiseuille flow in pipes, annuli, and channels. *Q. Appl. Maths* **26** (4), 575–599.
- JOSEPH, D.D. & TAO, L.N. 1963 Transverse velocity components in fully developed unsteady flows. *J. Appl. Mech.* **30** (1), 147–148.
- KALUR, A., SEILER, P. & HEMATI, M.S. 2021 Nonlinear stability analysis of transitional flows using quadratic constraints. *Phys. Rev. Fluids* **6** (4), 1–20. [arXiv:2004.05440](https://arxiv.org/abs/2004.05440).
- KERSWELL, R.R. 2018 Nonlinear nonmodal stability theory. *Annu. Rev. Fluid Mech.* **50** (1), 319–345.
- KERSWELL, R.R., PRINGLE, C.C.T. & WILLIS, A.P. 2014 An optimization approach for analysing nonlinear stability with transition to turbulence in fluids as an exemplar. *Rep. Prog. Phys.* **77** (8), 085901.
- KHODADADI, L., SAMADI, B. & KHALOOZADEH, H. 2014 Estimation of region of attraction for polynomial nonlinear systems: a numerical method. *ISA Trans.* **53** (1), 25–32.
- KREISS, G., LUNDBLADH, A. & HENNINGSON, D.S. 1994 Bounds for threshold amplitudes in subcritical shear flows. *J. Fluid Mech.* **270**, 175–198.
- LIU, C. & GAYME, D.F. 2020 Input-output inspired method for permissible perturbation amplitude of transitional wall-bounded shear flows. *Phys. Rev. E* **102** (6), 1–16. [arXiv:2006.16484](https://arxiv.org/abs/2006.16484).
- LIU, C. & GAYME, D.F. 2021 Structured input-output analysis of transitional wall-bounded flows. *J. Fluid Mech.* **927**(1992),
- LÖFBERG, J. 2004 YALMIP : A toolbox for modeling and optimization in MATLAB. In *2004 IEEE International Conference on Robotics and Automation (IEEE Cat. No.04CH37508)*, Taipei, Taiwan, pp. 284–289.
- LUNDBLADH, A., HENNINGSON, D.S. & REDDY, S.C. 1994 *Threshold Amplitudes for Transition in Channel Flows*. pp. 309–318. Springer Netherlands.
- MENG, F., WANG, D., YANG, P., XIE, G. & GUO, F. 2020 Application of sum-of-squares method in estimation of region of attraction for nonlinear polynomial systems. *IEEE Access* **8**, 14234–14243.
- MOFFATT, K. 1990 *Whither Turbulence, Chap. Fixed Points of Turbulent Dynamical Systems and Suppression of Nonlinearity*, pp. 250. Springer.
- NAGY, P.T. 2022 Enstrophy change of the Reynolds–Orr solution in channel flow. *Phys. Rev. E* **105** (3), 035108.
- NAGY, P.T. & KULCSÁR, M. 2023 Predicting the energy stability limit of shear flows using weighted velocity components. *Phys. Fluids* **35** (10), 104109.
- NAGY, P.T., PAÁL, G. & KISS, M. 2023 Imposing a constraint on the discrete Reynolds–Orr equation demonstrated in shear flows. *Phys. Fluids* **35** (3), 034115.

- NERLI, A., CAMARRI, S. & SALVETTI, M.V. 2007 A conditional stability criterion based on generalised energies. *J. Fluid Mech.* **581**, 277–286.
- NOCEDAL, J. & WRIGHT, S.J. 2006 *Numerical Optimization*. Springer.
- ORR, W.M.F. 1907 The stability or instability of the steady motions of a perfect liquid and of a viscous liquid. Part II: a viscous liquid. *Proc. R. Irish Acad.* **27**, 69–138.
- ORSZAG, S.A. 1971 Accurate solution of the Orr–Sommerfeld stability equation. *J. Fluid Mech.* **50** (4), 689–703.
- PAPACHRISTODOULOU, A., ANDERSON, J., VALMORBIDA, G., PRAJNA, S., SEILER, P. & PARRILO, P.A. 2013 SOSTOOLS: sum of squares optimization toolbox for MATLAB. Available at: <http://arxiv.org/abs/1310.4716>
- PARENTE, E., ROBINET, J.-C., DE PALMA, P. & CHERUBINI, S. 2022 Minimal energy thresholds for sustained turbulent bands in channel flow. *J. Fluid Mech.* **942**, A18.
- PERSHIN, A., BEAUME, C., EAVES, T.S. & TOBIAS, S.M. 2022 Optimizing the control of transition to turbulence using a Bayesian method. *J. Fluid Mech.* **941**, A25.
- PERSHIN, A., BEAUME, C. & TOBIAS, S.M. 2020 A probabilistic protocol for the assessment of transition and control. *J. Fluid Mech.* **895**, A16.
- PRIGENT, A., GRÉGOIRE, G., CHATÉ, H. & DAUCHOT, O. 2003 Long-wavelength modulation of turbulent shear flows. *Physica D: Nonlinear Phenom.* **174** (1), 100–113. papers from the Workshop on the Complex Ginzburg–Landau Equation: Theoretical Analysis and Experimental Applications in the Dynamics of Extended Systems.
- PRINGLE, C.C.T., WILLIS, A.P. & KERSWELL, R.R. 2012 Minimal seeds for shear flow turbulence: using nonlinear transient growth to touch the edge of chaos. *J. Fluid Mech.* **702**, 415–443.
- RABIN, S.M.E., CAULFIELD, C.P. & KERSWELL, R.R. 2012 Triggering turbulence efficiently in plane Couette flow. *J. Fluid Mech.* **712**, 244–272.
- REDDY, S.C., SCHMID, P.J., BAGGETT, J.S. & HENNINGSON, D.S. 1998 On stability of streamwise streaks and transition thresholds in plane channel flows. *J. Fluid Mech.* **365**, 269–303.
- REYNOLDS, O. 1895 On the dynamical theory of incompressible viscous fluids and the determination of the criterion. *Phil. Trans. R. Soc. Lond. (A)* **186**, 123–164.
- SCHMID, P. & HENNINGSON, S.D. 2001 *Stability and Transition in Shear Flows*. vol. 142. Springer.
- SCHMID, P.J. 2007 Nonmodal stability theory. *Annu. Rev. Fluid Mech.* **39** (1), 129–162.
- SERRIN, J. 1959 On the stability of viscous fluid motions. *Arch. Ration. Mech. Anal.* **3** (1), 1–13.
- STRAUGHAN, B. 2004 The energy method, stability, and nonlinear convection. In *Applied Mathematical Sciences*, vol. 91. Springer New York.
- SYNGE, J.L. 1938 Hydrodynamic stability. In *Proceedings of the Fifth International Congress for Applied Mechanics*.
- TAN, W. & PACKARD, A. 2008 Stability region analysis using polynomial and composite polynomial Lyapunov functions and sum-of-squares programming. *IEEE Trans. Autom. Control* **53** (2), 565–571.
- TOPCU, U., PACKARD, A. & SEILER, P. 2008 Local stability analysis using simulations and sum-of-squares programming. *Automatica* **44** (10), 2669–2675.
- TOSO, L.F., DRUMMOND, R. & DUNCAN, S.R. 2022 Regional stability analysis of transitional fluid flows. *IEEE Control Syst. Lett.* **6**, 2287–2292.
- TREFETHEN, L.N. & EMBREE, M. 2005 *Spectra and Pseudospectra*. Princeton University Press.
- VAVALIARIS, C., BENEITEZ, M. & HENNINGSON, D.S. 2020 Optimal perturbations and transition energy thresholds in boundary layer shear flows. *Phys. Rev. Fluids* **5** (6), 062401.
- WALEFFE, F. 1995 Transition in shear flows. Nonlinear normality versus non-normal linearity. *Phys. Fluids* **7** (12), 3060–3066.
- WALEFFE, F. 1997 On a self-sustaining process in shear flows. *Phys. Fluids* **9** (4), 883–900.
- WU, X. 2023 New insights into turbulent spots. *Annu. Rev. Fluid Mech.* **55** (1), 45–75.
- ZHANG, L. & TAO, J. 2023 Nonlinear optimal perturbations and formation mechanism of localized wave packet in channel flow. *Phys. Fluids* **35** (5), 051704.